

## Distinct accretion modes of Cygnus X-1 revealed from hard X-rays

PIOTR LUBIŃSKI <sup>1</sup>, ALEXANDROS FILOTHODOROS <sup>1</sup>, ANDRZEJ A. ZDZIARSKI <sup>2</sup> AND GUY POOLEY<sup>3</sup>

<sup>1</sup>*Institute of Physics, University of Zielona Góra, Licealna 9, PL-65-417 Zielona Góra, Poland*

<sup>2</sup>*Nicolaus Copernicus Astronomical Center, Polish Academy of Sciences, Bartycka 18, PL-00-716 Warszawa, Poland*

<sup>3</sup>*Astrophysics Group, Cavendish Laboratory, 19. J. J. Thomson Avenue, Cambridge CB3 0HE, UK*

(Received; Revised; Accepted)

Submitted to ApJ

### ABSTRACT

Thanks to recurrent observations of the black hole binary Cyg X-1 carried out over 15 years the *INTEGRAL* satellite has collected the largest data set in the hard X-ray band for this source. We have analyzed these data, complemented by data collected by other X-ray satellites and radio flux at 15 GHz. To characterize the spectral and variability properties of the system we have examined parameters such as the hard X-ray flux, photon index and fractional variability. Our main result is that the 2D distribution of the photon index and flux determined for the 22–100 keV band forms six clusters. This result, interpreted within the Comptonization scenario as the dominant process responsible for the hard X-ray emission, leads to a conclusion that the hot plasma in Cyg X-1 takes the form of six specific geometries. The distinct character of each of these plasma states is reinforced by their different X-ray and radio variability patterns. In particular, the hardest and softest plasma states show no short-term flux - photon index correlation typical for the four other states, implying a lack of interaction between the plasma and accretion disk. The system evolves between these two extreme states, with the spectral slope regulated by a variable cooling of the plasma by the disk photons.

*Keywords:* stars: black holes, X-rays: binaries — X-rays: individual (Cygnus X-1)

### 1. INTRODUCTION

Binary systems hosting a black hole (BH) can be subdivided into persistent and much more numerous transient sources (e.g., [Tetarenko et al. 2016](#)). Both classes are observed in several X-ray spectral states, followed by distinct properties of the emission from radio to UV bands (e.g., [Belloni & Motta 2016](#)). The three basic states are the soft (or high) state (SS) with a stronger soft X-ray emission, the hard (or low) state (HS) when the hard X-ray emission dominates, and the intermediate state (IS) corresponding to a transition between the two other states. There is a consensus that these states are associated with various arrangements of the accretion disk, plasma region(s) and outflowing material, the last in the form of jets or winds (e.g., [Fender & Muñoz-Darias 2016](#)). However, there are many different propo-

sitions of the actual scenario of the system’s geometry evolution. Prevailing are those invoking a varying inner radius of the disk as a main driver of the system changes (e.g., [Esin et al. 1997](#)), i.e., related to the advection-dominated accretion flow (ADAF) models ([Narayan & Yi 1994](#); [Abramowicz et al. 1995](#)) with a hot inner flow replacing the disk. Alternative to the truncated disk scenario are, for example, models with a magnetized disk of constant size where the state transitions result from a varying strength of the toroidal component of the disk field ([Begelman et al. 2015](#)).

Studies of spectral states of BH binaries (BHB) were intensified in the mid-1990s when the Rossi X-ray Timing Explorer (*RXTE*, [Bradt et al. 1993](#)) started operation. Besides a detailed modeling of the high-quality spectra there were several phenomenological tools developed: the hardness-intensity diagrams (HIDs), the fractional rms variability (RMS)-intensity diagrams, and the hardness-RMS diagrams (HRD). Whereas transient BHBs typically follow the so-called q-shaped track in

HID, persistent BHBs show rather only a fraction of that track (Belloni & Motta 2016).

Varying energy spectra and variability explored through the RMS, power-density spectra (PDS), coherence and lags studies resulted in an extension of the state classification. Many transient sources exhibit a phase of very strong disk emission coupled with a prominent steep power-law continuum at higher energies, so-called very high state or steep power-law state (VHS, e.g., McClintock & Remillard 2006). Transitions between the SS and HS states were found to show two different phases, introducing the soft intermediate (SIMS) and hard intermediate (HIMS) states instead of a single IS for transient systems (e.g., Belloni 2010).

An unambiguous, though simple way of state classification is vital to get deeper insights on the physics of accreting BHBs. The most reliable selection is usually obtained with the criteria based on color-color or slope-slope diagrams, whenever the X-ray spectra are available (e.g. Zdziarski et al. 2002; Wilms et al. 2006; Gierliński et al. 2010). Nevertheless, to fully explore the evolution of both transient and persistent systems, the X-ray monitoring data and HRD-based selection must be applied, at the expense of a somewhat weaker identification of the intermediate state (Grinberg et al. 2013).

Cyg X-1, the first BHB detected (Bowyer et al. 1965) and one of the brightest, persistent hard X-ray sources, hosts a black hole and a blue supergiant HD 226868. Thanks to the brightness of Cyg X-1, a wealth of information about its nature has been gathered. However, being one of only several known high-mass wind-fed persistent BHBs, it might be not quite representative of the BHB class in general. Indeed, the HID diagram for Cyg X-1 does not show a typical q-track, occupying only a part of the region covered typically by the transient systems (Belloni 2010). This can be related to a relatively small range of the bolometric luminosity observed for this source, varying by a factor  $\lesssim 10$  (Wilms et al. 2006; Zdziarski et al. 2011). The transitions between the soft and hard state occur at the same flux level in both directions, whereas the transient systems display a hysteresis behavior. Moreover, during the soft state Cyg X-1 does not reach very low level of rms variability, typical of that state in other systems (Belloni 2010).

Variability studies at soft X-rays revealed that the hard state in which Cyg X-1 is observed for most of the time changed for a quite long period into a slightly softer hard state, showing a number of failed transitions into the soft state (Pottschmidt et al. 2003a). Cyg X-1 belongs to the anomalous track class, exhibiting a stronger radio-soft X-ray correlation than that typically observed for the transient BHBs (Zdziarski et al. 2011). In the

hard X-ray band this correlation becomes more complex, with the highest radio emission observed for medium X-ray fluxes (Wilms et al. 2006; Zdziarski et al. 2011).

The vast majority of extensive studies of Cyg X-1 spectral states was based on the *RXTE* data, predominantly limited to the 3–35 keV band. Emission in this band is commonly thought to be a mixture of the primary emission of the disk and hot plasma, accompanied by Compton reflection of the plasma radiation from the disk. Therefore, an interpretation of the results in terms of a complex physical model is usually demanding. On the other hand, the emission in the 22–100 keV band is dominated by the Comptonized continuum (see fig 2 of Filothodoros et al. 2018), allowing for a more direct analysis of the plasma properties. There were many spectral studies of the hard X-ray band exploring high-quality data from pointed observations (e.g. Gierliński et al. 1997; Del Santo et al. 2013) and various examples of a comprehensive analysis of a large data set covering a long period (e.g., Gleissner et al. 2004; Zdziarski et al. 2011).

*INTEGRAL* satellite (Winkler et al. 2003) observations provided a variety of valuable information on the nature of Cyg X-1 (e.g. Pottschmidt et al. 2003b; Zdziarski et al. 2012; Del Santo et al. 2013). *INTEGRAL*'s uninterrupted observation (science window) typically lasts 0.5–2 hours and the sensitivity of the ISGRI detector (Lebrun et al. 2003) allows one to obtain, within this period, data of a quality surpassing the daily-averaged data from the hard X-ray monitors. This motivated us to perform an extensive analysis of the spectral states of Cyg X-1, based on the hard X-ray emission. A detailed analysis of the state-wise summed spectra with advanced Comptonization models must be postponed until the improved ISGRI calibration (OSA 11, see Sec. 2.1) is extended to the entire mission period.

## 2. DATA SELECTION AND REDUCTION

### 2.1. *INTEGRAL*

Our analysis utilizes all public *INTEGRAL* data released before March 1, 2018. These data were collected during the spacecraft orbits (revolutions, Revs), ranging from 22 up to 1882, i.e., within a period between 2002-12-18 08:55:11 UTC and 2017-11-08 03:04:31 UTC. *INTEGRAL* data were reduced with the OSA software package (Courvoisier et al. 2003), version 10.2 (ISGRI and SPI detectors) and version 11.0 (JEM-X 1 detector).

To investigate the hard X-ray properties of the spectral states of Cyg X-1 we used a large dataset collected by the ISGRI detector in the 22–100 keV band. A main tool to study the spectral states is the hardness-intensity diagram. However, the hardness ratios depend strongly

on the choice of the two energy bands. On the other hand, there are substantial changes of the ISGRI characteristics observed over the considered 15 years (Natalucci & Savchenko 2017). For this reason, we decided to use the photon index of a power-law model fitted to the 22–100 keV spectra instead of the hardness ratio. We have also computed the flux in the same band based on the fitted model. In this way, by applying a set of time dependent instrument responses we have reduced the influence of the evolution of the ISGRI detector on both our basic parameters, characterizing the intensity and spectral slope.

The ancillary calibration files (ARFs) of OSA 10.2 for ISGRI were released in December 2015 and are not appropriate for data collected more than several months afterwards. To enable using data collected during the last two years of the analyzed period, we prepared our own spectral calibration. A set of 5 ARFs was generated by inverting the Crab spectra collected during the years 2016 and 2017, to ensure an overall agreement with the INTEGRAL’s standard model of the Crab spectrum, based on the SPI detector results (Jourdain et al. 2008). Although this approach can be insufficient for a detailed spectral analysis with complex models, it ensures a good correction of the fluxes measured in relatively wide energy band.

The new OSA package, version 11, was released on October 19, 2018 and is valid only for the Cyg X-1 observations between Revs. 1626 and 1882. Using Crab observations from Revs. 1662–1887 we compared spectral fits obtained for OSA 10.2 with our ARFs and with OSA 11. Typically the Crab photon index in the 30–100 keV band from OSA 11 is less by 0.02–0.03 than the photon index fitted to the OSA 10.2 spectra. This difference is a result of the new Crab spectral model adopted for OSA 11<sup>1</sup>, with the reference photon index of 2.1 instead of 2.08 used before (Jourdain et al. 2008). We observe a similar effect of an overall spectral softening for Cyg X-1 data taken during the OSA 11 validity period. To avoid mixing various calibration versions for this project we used only OSA 10.2, with our ARFs for the recent observations.

The selection of the ISGRI data was based on a criterion of at least 10% of the detector area being illuminated by Cyg X-1, which corresponds roughly to observations with an off-axis angle  $< 15^\circ$ . This resulted in 8128 science windows filtered with the OSA software. For further analysis we selected 7907 science windows with a relative uncertainty of the count rate in the 22–

100 keV band  $< 10\%$ . For each of them we extracted a 6-channel spectrum (with energy limits: 22.1–25.0–30.2–40.3–52.7–70.4–100.1 keV), analyzed later with the XSPEC fitting code, version 12.9.0n. The spectra were fitted with a power-law model, convolved with the `cf1lux` model to compute the flux and its uncertainty. The results are the hard X-ray photon index  $\Gamma_H$  and the flux  $F_H$  integrated in the 22–100 keV band. After this step, in order to reduce the uncertainty of the points in the  $\Gamma_H$ - $F_H$  diagram we excluded all results with a relative  $\Gamma_H$  error  $> 10\%$ , obtaining 7844 science windows. Finally, we also excluded 23 science windows collected during revolutions 1554–1557 when the count rate of the outbursting V404 Cygni in the 22–40 keV band was higher than 1000 cps. After applying all the selection criteria the final data set consisted of 7821 science windows, with a total exposure time of 18.53 Ms (covering 3.9% of the entire studied period) and about 2.1 billion photons emitted by Cyg X-1 in the 22–100 keV band. The neglected low-quality data correspond mostly to the soft state, decreasing its population by about 20%. As we have tested, an exclusion of those 307 science windows does not introduce any bias in our results.

Despite their relatively low sensitivity, the JEM-X detectors ensure exactly contemporary observations to the ISGRI detector. The JEM-X field of view is smaller than that of IBIS and we have used only data from observations when the source off-axis angle was below  $5^\circ$ . Tests done with the Crab data revealed a small discrepancy between the hardness ratios of both JEM-X detectors. To avoid artifacts when mixing the JEM-X 1 and JEM-X 2 results we decided to use only JEM-X 1 data. We have used the standard OSA 11.0 software settings except for switching off the “skipSPEfirstScw” option and filtered out 2992 good science windows. The light curves of JEM-X 1 detector were extracted in two energy bands: 3–5 keV and 5–12 keV.

In the case of the SPI detector we used the `spiros` software included in OSA 10.2, set to the SPECTRA mode. Each spectrum was extracted with 6 linear energy channels in the 22–100 keV band. The background was estimated using the GEDSAT background model. The other options of the `spi.science.analysis` routine were set to their default values and all known bad pointings were automatically ignored. In total, 7772 single science window spectra were fitted with a power-law model. The sensitivity of SPI below 100 keV is lower than that of ISGRI and for this reason we had to exclude a much larger fraction of data. After a selection based on the photon index uncertainty  $\leq 0.1$ , 2894 science windows were used for further analysis.

<sup>1</sup> L. Natalucci, private communication.

## 2.2. Other observatories

Since the spectral state classification of Cyg X-1 is usually based on analysis of the X-ray data below  $\approx 20$  keV, *INTEGRAL*'s data have to be complemented by data taken by other X-ray observatories. In addition, to deepen our analysis we have also used radio data from a contemporary monitoring of Cyg X-1.

The All-Sky Monitor (ASM, Levine et al. 1996) on board the *RXTE* satellite monitored Cyg X-1 in the 1.5–12 keV band. We have used the data in the three ASM sub-bands, 1.5–3 keV, 3–5 keV and 5–12 keV, taken from the ASM Archive<sup>2</sup> covering the period contemporary to *INTEGRAL*'s observations, MJD 52626 – MJD 55200 (the ASM data taken after MJD 55200 were ignored, see Grinberg et al. 2013). Depending on our purposes, we used either the orbital or daily-averaged data.

After the *RXTE* mission completion the main instrument used for the soft X-ray monitoring is the Monitor of All-sky X-ray Image (MAXI, Matsuoka et al. 2009) on board the International Space Station. MAXI provides data in three energy bands: 2–4 keV, 4–10 keV and 10–20 keV. We used both the orbital and daily-averaged data, downloaded from the mission archive<sup>3</sup>. The daily-averaged spectra of the MAXI's Gas Slit Camera (GSC) were extracted with the `mxproduct` tool included in the HEASOFT package (Matsuoka et al. 2009).

BATSE data were downloaded from the Earth Occultation Data Products archive<sup>4</sup>. The daily spectra were extracted following the Earth occultation analysis described in Harmon et al. (2004). We have used the HEASOFT `bod2pha` tool, setting the minimum number of flux determinations to 4 for each module of the large-area detector (LAD). The spectral response for each viewing period and each LAD module was generated with the HEASOFT `bod2rmf` tool. In total, we got 2728 daily spectra for a period between May 2, 1991 and September 15, 1999. The spectra of each LAD module were fitted together in the 22–100 keV band with a power-law model. The photon index for a given day was computed as a weighted mean of photon indices fitted to all individual module spectra.

The BAT detector (Krimm et al. 2013) on board the Neil Gehrels *Swift* satellite (Gehrels et al. 2004) operates in an energy band similar to *INTEGRAL*'s ISGRI, namely 14–195 keV. Its sensitivity is slightly lower than that of ISGRI and its mean exposure time for a single day monitoring of Cyg X-1 is  $91 \pm 70$  minutes, i.e. of the

order of typical duration of a single *INTEGRAL* science window. We used BAT's continuous monitoring data in the 15–50 keV band<sup>5</sup>.

The largest radio dataset of the Cyg X-1 monitoring contemporary to the *INTEGRAL* mission is that collected by the Ryle Telescope (RT, Jones 1991, before MJD 53903) and its successor, the Arcminute Microkelvin Imager (AMI, Zwart et al. 2008, after MJD 54752). The RT bandwidth was 0.35 GHz at 15 GHz, whereas AMI covers a frequency range between 13.5 – 18 GHz, also centered at 15 GHz. A typical exposure time was  $\approx 10$  minutes and Cyg X-1 was observed  $\approx 10$  times per day. The Ryle and AMI data that we use here were already published by Zdziarski et al. (2017); Zdziarski et al. (2020).

## 3. RESULTS

### 3.1. Long-term variability of Cyg X-1

In Fig. 1 we present several parameters derived from the data collected by the ISGRI, ASM, MAXI, and BAT detectors together with the radio flux measured by RT and AMI for a period of the Cyg X-1 monitoring analyzed by us (MJD from 52626 to 58065). All data were rebinned to a 1-day time bin. The points are colored according to the state selection of Grinberg et al. (2013) (see their table 2). Using joint ASM+MAXI data we computed that the source spent 64%, 10% and 26% of the time in the hard, intermediate and soft state, respectively.

In panels (a) and (b) of Fig. 1 the ASM (5–12/1.5–3) keV hardness and the MAXI (4–10/2–4) keV hardness are shown, respectively, both being good tracers of the system state. The other panels of Fig. 1 present the *Swift*/BAT flux in the 15–50 keV band (c), the ISGRI 22–100 keV flux  $F_H$  (d) and photon index  $\Gamma_H$  (e), and the RT/AMI 15 GHz flux (f). As shown in fig. 7 of Grinberg et al. (2013), the intermediate state region defined for MAXI is relatively narrow and this is seen also in our results, with a quite narrow band of intermediate data in Fig. 1(b). For this reason there are several periods after MJD 55400 during which the soft state selected with MAXI corresponds to a hard X-ray (BAT) and radio emission observed at levels typically seen during the intermediate or hard state. Taking into account energy bands other than the soft X-ray band, Fig. 1 demonstrates that the hard X-ray photon index is a very good indicator of the hard state, whereas the radio and hard X-ray fluxes are valuable for the soft state selection.

<sup>2</sup> <http://xte.mit.edu/asmlc/ASM.html>

<sup>3</sup> <http://maxi.riken.jp/sugizaki/v51/>

<sup>4</sup> <https://heasarc.gsfc.nasa.gov/docs/cgro/batse/>

<sup>5</sup> <https://swift.gsfc.nasa.gov/results/transients>

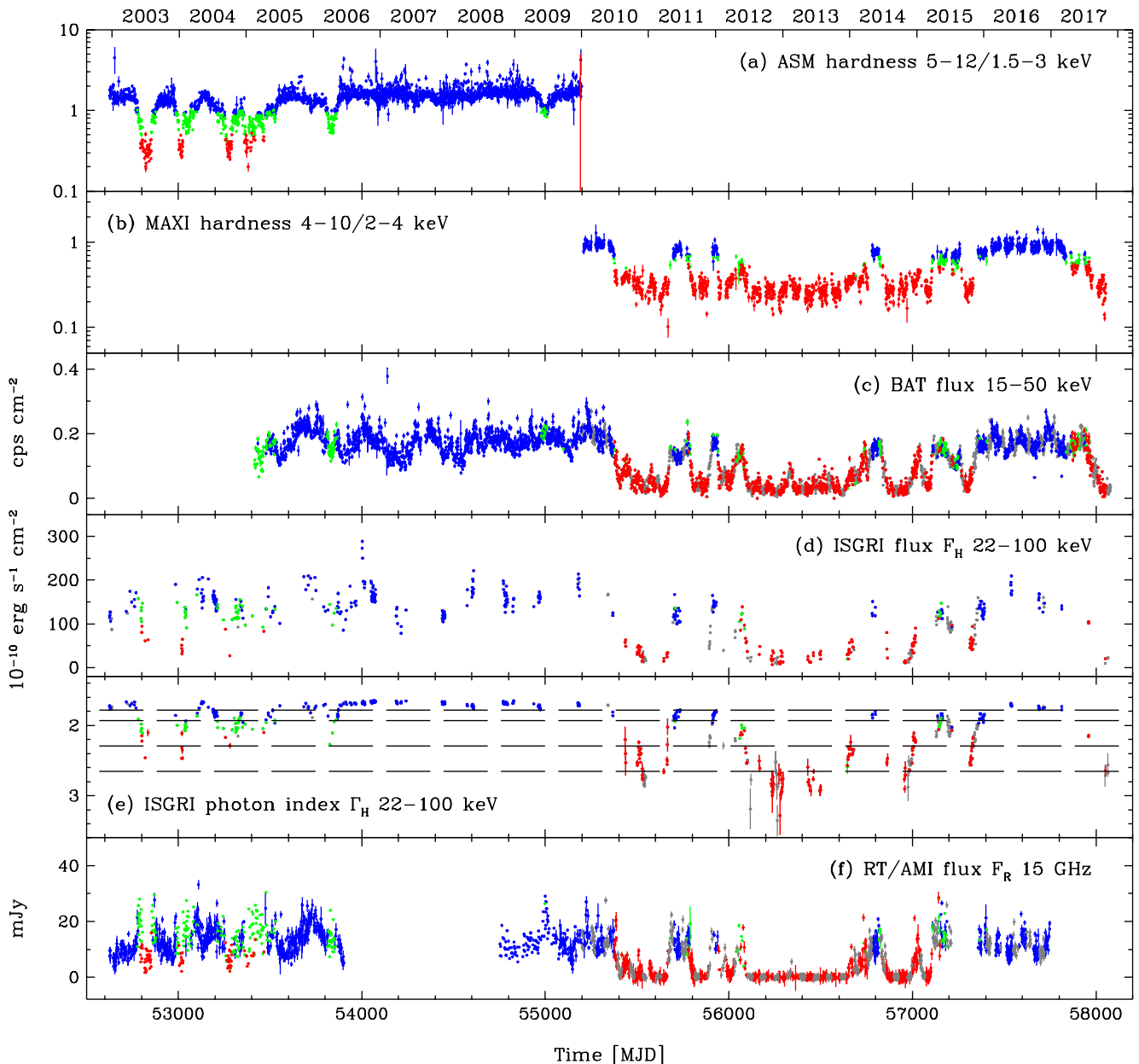


**Figure 1.** Light curves and other spectral parameters of the Cyg X-1 emission obtained with various observatories during the studied period. All data are extracted for a time bin of one day. Color coding corresponds to the [Grinberg et al. \(2013\)](#) state classification, based on ASM data up to MJD 55200 and MAXI data after that day: hard (blue), intermediate (green) and soft (red). Grey color shows data unclassified due to the MAXI gaps. Dashed lines in panel (e) mark the limits of the plasma states (see Sec. 3.2).

### 3.2. Plasma states in Cyg X-1

Figure 2 presents the ISGRI 22–100 keV flux  $F_H$  as a function of the best-fit photon index  $\Gamma_H$  of the power-law model fitted in the same band to the single science window spectra. We use this plot as a hard X-rays counterpart of a HID used to study spectral evolution of various binary systems in the soft X-rays band. In general, data shown in Fig. 2 form two distinct regions, a rela-

tively well concentrated high-flux region corresponding to the hard state and a major part of the intermediate state, and a much more dispersed region corresponding to the soft state.

To better visualize the data clustering and reveal some features of the  $\Gamma_H$ - $F_H$  distribution we have computed its 2-D density map, presented in Fig. 3. The density of data points was computed for pixels separated by  $\Delta\Gamma_H = 0.005$  and  $\Delta\log(F_H) = 0.007$ , over an ellipse with the

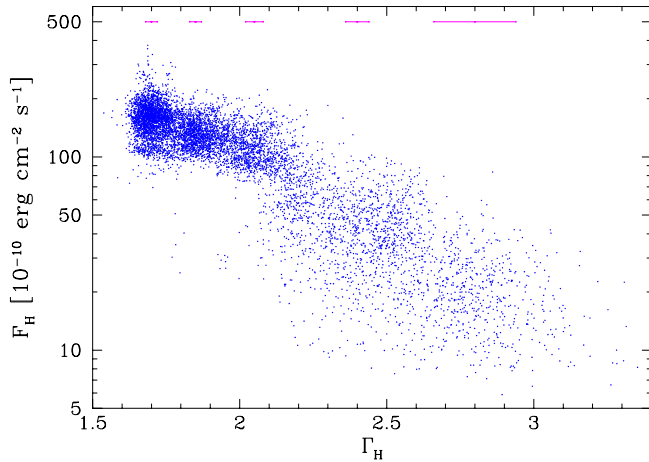


**Figure 2.** ISGRI flux in the 22–100 keV band,  $F_H$ , plotted against the photon index  $\Gamma_H$  characterizing the single science window spectra in the same energy band. Magenta lines show typical  $\Gamma_H$  errorbars at several  $\Gamma_H$  values (errors of  $F_H$  are very small, of the line width size).

$\Gamma_H$  and  $F_H$  semiaxes 10 times larger than the pixel separation. We tried several options of the pixel distances and integration region sizes, choosing the one best showing both local density peaks and the regions edges or valleys between them. Also the color coding was adjusted to reveal those features with a rather contrasted instead of smoothly transiting shades.

The density map shown in Fig. 3 reveals two main regions, the hard and soft regimes, well separated by the flux level of  $75 \times 10^{-10} \text{ erg cm}^{-2} \text{ s}^{-1}$ . In both regimes we observe three subregions, forming two sharp peaks for  $\Gamma_H < 1.93$ , two flatter ridges in the soft-hard transition region ( $1.93 < \Gamma_H < 2.29$ ) and two dispersed peaks for the soft data ( $\Gamma_H > 2.29$ ). From now we call these regions: pure hard (PH), transitional hard (TH), hard intermediate (HI), soft intermediate (SI), transitional soft (TS) and pure soft (PS) states, respectively, with the exact  $\Gamma_H$  and  $F_H$  limits provided in Table 1. This nomenclature and adopted limits will be explained in Secs 3.3 and 3.4, where various properties of these states are discussed.

Since this is the first time when such a clustering of parameters describing the plasma in the accreting BH system is presented, we have to examine its reliability. There is a variety of simple heuristic clustering tests but most of them lack means to assess a relative probability between the hypotheses of different numbers of clusters. This limitation can be solved by using methods based on the probability density models with the Bayes Information Criterion applied to discriminate between those models (Fraley & Raftery 2002). In case of our data a construction of such density models can be demanding

due to the, possibly, non-Gaussian shape of the regions. However, for such high density gradients and quite regular shapes as observed in Fig. 3 those methods should confirm the presence of at least five clusters (except for HI state). To prove this we have made a simple estimate of the probability that the low-density valley seen between the two soft state regions appears by a chance.

The solid line in Fig. 3 connects the centers of these two soft state regions. The valley is more or less perpendicular to this gradient line. We have computed the numbers of data falling into rectangular regions with centers located along this line. Two examples of such regions are shown in Fig. 3. We have tested several sizes of these rectangles. An example of the results of this density gradient study is presented in Appendix A. As a null hypothesis (a single soft state) we applied several options of a pure or deformed Gaussian density distribution. If these models describe data, there are about 60 points missing in the valley (see Fig. 10). These points must be shifted by a statistical fluctuation to the one of the peak regions. As shown in Fig. 2, typical  $1-\sigma$  uncertainty of  $\Gamma_H$  in this region of the diagram is about 0.1, i.e., slightly smaller than the expected shift. Thus an upper limit for a probability that a single point is shifted from the valley to one of the peaks corresponds to  $1-\sigma$  probability, 0.32. Hence the joint probability of such coherent fluctuation of the position of 60 points in the diagram will be smaller than  $(0.32)^{60} \approx 2 \times 10^{-30}$ .

For the other pairs of neighboring regions seen in Fig. 3 the density gradients between them are similar or stronger in terms of the number of points that must be shifted (note the log-scale of the density). In addition, they have to be shifted by more than several  $\sigma$ 's (see errorbars in Fig. 2), thus their separation must be statistically highly probable. The only exception is the hard intermediate state region appearing as an extension of the hard state region (but see the Fig. 3 insert showing a better separation). In Secs 3.3 and 3.4 we demonstrate that this region exhibits several properties distinct from those of the two hard states.

Besides purely statistical fluctuations we considered an issue of our simplistic spectral model in a form of the power-law. Neglecting the continuum curvature due to the Compton reflection, high-energy cut-off and other effects can lead to an artificial photon index clustering. In Filothodoros et al. (2018) almost the same *INTEGRAL* data set was analyzed through spectral fitting of a hybrid Comptonization model `eqpair`. Using their results we performed a test to check if the power-law model fitted to the spectra simulated with a realistic shape changing smoothly with the spectral hardness can induce a spurious aggregation of the  $\Gamma_H$  values. The test

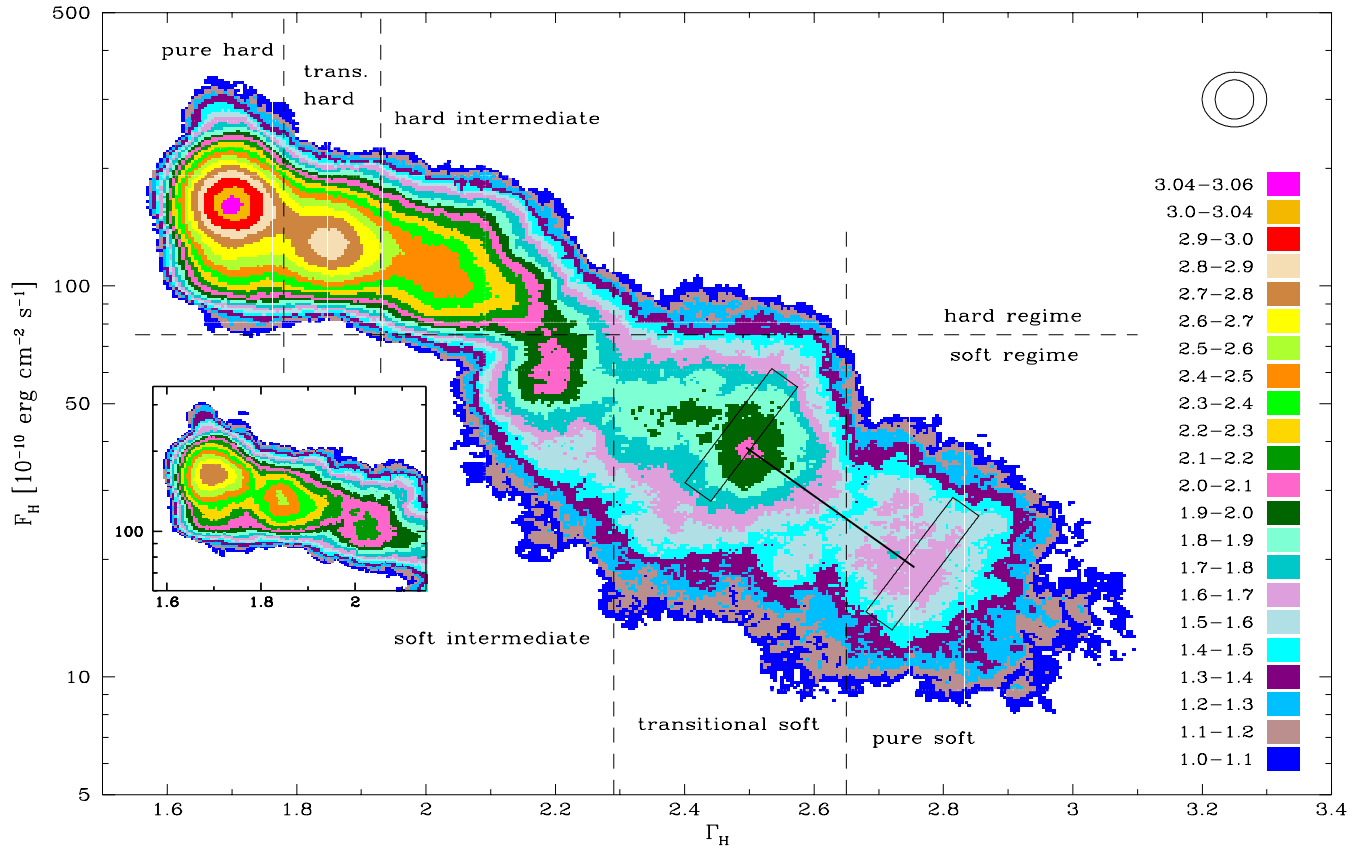


**Figure 3.** Density map of the  $\Gamma_{\text{H}} - F_{\text{H}}$  diagram, color coding corresponds to the logarithm of the number of data within a region centered at a given pixel. A larger ellipse above the colorbar shows the size of that region. The vertical dashed lines mark the borders of the six plasma states, horizontal dashed line marks the hard/soft regime border. The solid line connecting the centers of the two soft state regions is shown together with two examples of the rectangular regions used to compute the density gradient (see the text). The insert shows a density map for the three hard states computed with a finer sampling region (smaller ellipse over the colorbar).

details and results are presented in Appendix B. Simulations demonstrated that the  $\Gamma_{\text{H}}$  distribution is modified by varying all main parameters of the `eqpair` model, not only those controlling the reflection and high-energy cut-off. Nevertheless, our test demonstrated that an approximation of the spectral shape with the power-law model does not introduce any specific  $\Gamma_{\text{H}}$  aggregation. Thus, our clustering results turn out to be essentially free from both statistical and systematic effects.

In the rest of this section and Secs 3.3 and 3.4 we consider several other parameters characterizing the Cyg X-1 emission, showing that they expose in various ways the distinct nature of the six states found with the  $\Gamma_{\text{H}} - F_{\text{H}}$  density diagram. Figures 4 and 5 present these parameters as a function of  $\Gamma_{\text{H}}$  and  $F_{\text{H}}$ , respectively. The corresponding Tables 1 and 2 summarize the results of statistical analysis of various properties of the six states, in terms of the mean values and correlations, respectively.

Although the density data in Fig. 3 for the hard and soft regimes depend on both  $\Gamma_{\text{H}}$  and  $F_{\text{H}}$ , the hard photon index is the primary parameter that enables the separation of the six states. In panel (e) of Fig. 4 we show the  $\Gamma_{\text{H}}$  distribution<sup>6</sup> and its decomposition into 6 Gaussians, providing a quite good approximation (reduced  $\chi^2$  around 1.2). This fit should be treated with a caution because the peaks shown in Fig. 3 are not quite symmetric and there is an overlap between both intermediate states. Therefore, we use the fitted curve only to guide the eye (see Sec. 3.6).

The first quantity confronted with  $\Gamma_{\text{H}}$  and  $F_{\text{H}}$  is the JEM-X 1 hardness ratio  $H_{\text{S}}$  (panel (a) of Figs. 4 and 5). The JEM-X 1 data should be corrected for the orbital modulated absorption, which can reach quite high values

<sup>6</sup> All single-parameter distributions shown in this paper are computed as the probability density functions, i.e., taking into account the abscissa units and normalized to give the total integral equal to 1.

(Grinberg et al. 2015). However, such a correction is not possible without a detailed spectral analysis, out of scope of this paper. When the JEM X-1 3–12 keV count rate data are plotted against the orbital phase (according to Gies et al. 2008), we do not see a clear general trend, either for the entire data set or state-wise selection. Therefore, we use uncorrected data, which introduces some scatter in the results.

As shown in Table 2, the hardness ratio  $H_S$  does not correlate with  $\Gamma_H$  for the PH and SI states, strongly anticorrelates for the TH, HI, and TS states and shows weak anticorrelation for the PS state. Correlations between  $F_H$  and  $H_S$  are positive and strong for the four softer states, very weak for TH state and weak for PH state. An important issue seen in Fig. 4(a) is that the soft X-ray hardness cannot be used to identify the six plasma states found by us due to a lack of a clear segregation of the  $H_S$  values. In particular, the PH and TH states cannot be separated and the three softest states are strongly mixed. The two intermediate states data between  $\Gamma_H = 1.93$  and  $2.29$  occupy different ranges of the  $H_S$  range, as shown in red in Fig. 4(a), however, this does not allow for a good separation.

### 3.3. Hard X-ray variability

#### 3.3.1. Fractional variability

The second fundamental diagram, besides the HID, commonly applied to characterize the behavior of BHBS is the hardness-rms diagram (e.g. Belloni 2010). To construct a similar diagram with the ISGRI data, we have computed a normalized fractional variability amplitude  $S_V$  expressed as

$$S_V = (\sigma_V / \bar{c}) \times 100\%, \quad (1)$$

with the fractional variability amplitude  $\sigma_V$  fulfilling an equation derived by Almaini et al. (2000)

$$\sum_{i=1}^N \frac{(c_i - \bar{c})^2 - (\sigma_i^2 + \sigma_V^2)}{(\sigma_i^2 + \sigma_V^2)^2} = 0, \quad (2)$$

where  $c_i$  is the count rate measured for a given time bin,  $\sigma_i$  is its statistical error,  $\bar{c}$  is the mean count rate for a given science window, and  $N$  is the number of time bins within the science window period.

The time bin adopted for this analysis was 1 minute. With this, a relative statistical uncertainty of the count rate for a single measurement was exceeding 50% only for about 3.6% of the data. On the other hand, since the *INTEGRAL* science window typically lasts at least 20 minutes, there were at least 20 time bins used to compute the  $S_V$  value for each science window. We have found that for 513 out of 7566 science windows

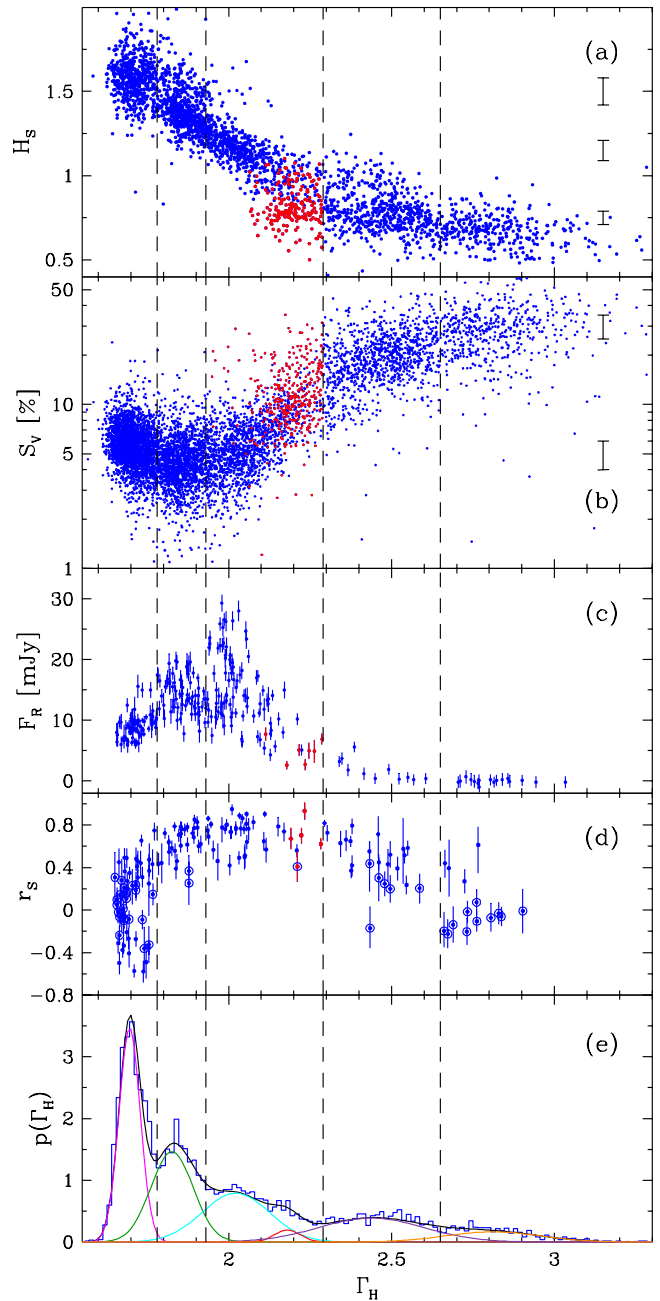


**Figure 4.** JEM-X 1 hardness ratio  $H_S$  (a), fractional variability amplitude  $S_V$  (b), radio flux  $F_R$  (c) and the Spearman coefficient  $r_S$  (d) plotted against the hard X-ray photon index  $\Gamma_H$ . The SI state data in panels (a)–(d) are shown in red. Vertical errorbars in panels (a) and (b) show typical errors of  $H_S$  and  $S_V$ , respectively, at a given level of these quantities. Circles in panel (d) mark data with the null hypothesis probability  $> 0.1$ . (e) Decomposition of the  $\Gamma_H$  distribution (blue) into a sum of six Gaussians (black). The Gaussians corresponding to the PH (magenta), TH (green), HI (cyan), SI (red), TS (violet) and PS state (orange) are also shown. The dashed lines mark the  $\Gamma_H$  limits of these six states, except for the HI and SI states occupying the same range (see Table 1).



the left side of Eq. 2 was positive even for  $\sigma_V = 0$ , i.e., the observed variability was smaller than purely statistical fluctuations. This indicates that the statistical error of the count rate determined with the OSA software is somewhat overestimated. For a 60 s exposure time a single ISGRI pixel registers usually 0 or 1 count from a source as bright as Cyg X-1. This is the lowest signal-to-noise regime, where the OSA software tends to slightly amplify the statistical errors (see the Appendix A in Lubiński 2009 for a discussion).

To estimate this excess we have extracted 1-minute light curve for the Crab, a relatively stable source with the count rate level similar to that of Cyg X-1 in the hard state. For Crab we have found that Eq. 2 cannot be fulfilled for 2380 out of 5582 science windows. Decreasing the statistical errors by a systematic 1% error reduced this number to 35. We have applied the same 1% correction to the Cyg X-1 data, reducing the number of non-determined  $\sigma_V$  values to 212 and excluding corresponding cases from a further  $S_V$  analysis. The uncertainty of  $S_V$  was determined with the bootstrap method, in a way following that of Soldi et al. (2014).

Figure 4(b) presents the results of variability analysis where the  $S_V$  amplitude is plotted against the  $\Gamma_H$  index. To the best of our knowledge this is the first time where such diagram is constructed with the data from the hard X-ray band.

Our analog of the soft X-ray HRD diagram presented in Fig. 4(b) extends the findings of Grinberg et al. (2014) to energies above 15 keV. A complete comparison is not possible because our  $S_V$  was extracted for roughly 0.5–8 mHz range, whereas their fractional rms was computed for the 0.125–256 Hz band and their  $\Gamma_1$  was fitted below  $\approx 10$  keV. Nevertheless, their result for the highest energy band, 9.3–15 keV, looks qualitatively similar to our result in a sense that the minimal variability is observed for medium hardness spectra. Main differences are the location of that minimum (our TH state vs. their relatively soft state) and their soft state variability higher than that of the hard state only for the softest data.

An analysis of Cyg X-1 *INTEGRAL* data in a much broader frequency range was presented by Cabanac et al. (2011), who analyzed variability in the 27–49, 69–90 and 96–130 keV bands with the SPI detector. Their frequency range was 1 mHz – 100 Hz, however, the data cover only the period from 2005 March to 2008 May, i.e., the period when Cyg X-1 was almost exclusively in the hard state (see Fig. 1). The rms amplitude found for that period increases with the spectral hardness (see fig. 4 of Cabanac et al. 2011), in agreement with our results shown in Fig. 4(b).

The intra-state  $\Gamma_H$ - $S_V$  correlation results presented in Table 2 confirm the trends seen in Fig. 4(b), i.e., anticorrelation in the PH state, lack of correlation for the TH and PS states, and positive correlation for the three other states. For the  $F_H$ - $S_V$  pair the situation is different: correlation for the PH state, clear correlation for TH state changing into strong anticorrelation for the next three states and no correlation for the PS state.

### 3.3.2. Short-term $\Gamma_H$ - $F_H$ correlations

Inspecting the single revolution data we noticed a clear and common  $\Gamma_H$ - $F_H$  correlation, not seen only for the two pure states. To explore this topic we applied the Spearman rank-order test to the  $\Gamma_H$ - $F_H$  data for each revolution with at least 10 science windows, in total 161 revolutions. The results of this investigation revealed that a coherent variability lasts longer than the revolution period for a majority of data but sometimes there is a jump observed between the two distinct correlation patterns. Thus, the characteristic period of the  $\Gamma_H$ - $F_H$  coherence is typically longer than several days. Definitely this issue needs a deeper study, which is out of the scope of our paper. Nevertheless, to clean the correlation results from these rapid jumps for each revolution we determined the longest period of an interrupted correlation (or its lack) characterized by the minimum (or maximum) of no correlation probability, neglecting the rest of this revolution data. Such a selection was needed for about half of revolutions and neglected fraction was typically below 20%.

The results of the Spearman test are shown in Figs 4(d) and 5(d), where the single revolution  $\Gamma_H$ - $F_H$  correlation coefficient  $r_S$  is plotted against the mean  $\Gamma_H$  and mean  $F_H$ , respectively, for a given revolution or part of it. We do not show the null hypothesis probability  $P_S$  in these two figures, however, the points corresponding to  $P_S > 0.1$  are marked with circles. The errors in  $r_S$  and  $P_S$  were computed through Monte-Carlo simulations, taking into account the  $\Gamma_H$  and  $F_H$  uncertainty. Note that the  $\Gamma_H$ - $r_S$  and  $F_H$ - $r_S$  correlation results presented in Table 2 were also computed for the revolution-averaged data because  $r_S$  is always computed for a single revolution, not a single science window. On the other hand, the  $\Gamma_H$ - $F_H$  correlation parameters in Table 2 are the long-term results, computed for all data for a given state.

The difference between the PH state results and the TH, HI, SI and TS states results is striking. For the PH state a positive, missing and negative correlations are possible and the no-correlation probability  $P_S$  is quite high (see Table 1). For data with the  $\Gamma_H$  between 1.78 and 2.65 there is a dramatic change: a clear positive cor-

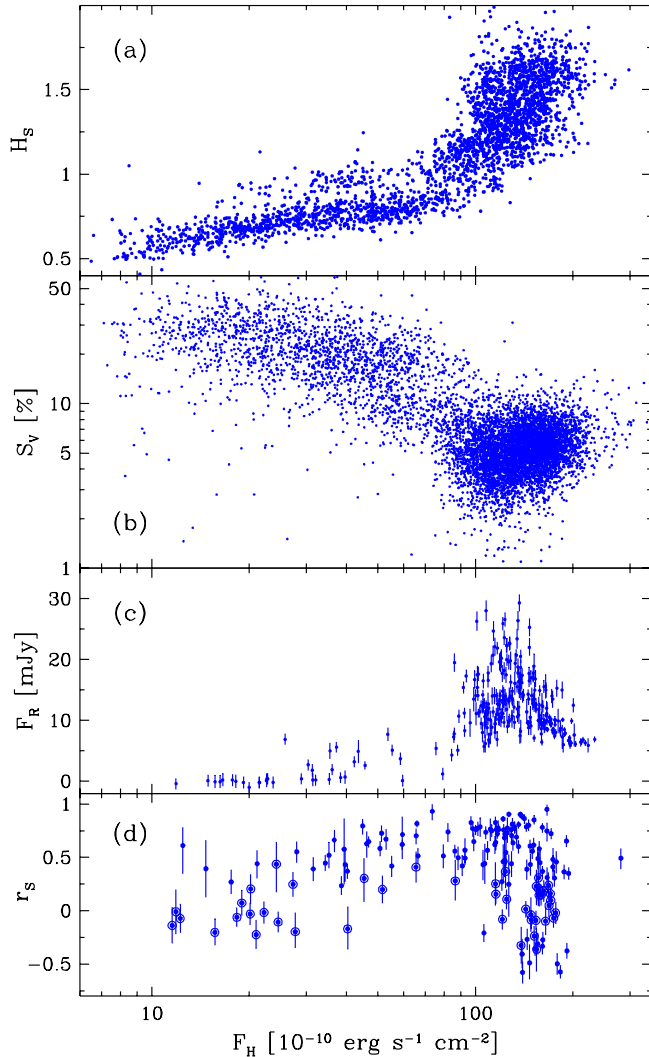


**Figure 5.** JEM-X 1 hardness ratio  $H_S$  (a), fractional variability amplitude  $S_V$  (b), radio flux at 15 GHz  $F_R$  (c) and the Spearman coefficient  $r_S$  (d) plotted against the hard X-ray flux  $F_H$ .

relation ( $r_S > 0.4$ ) is seen and the null hypothesis probability is usually close to 0. For the pure soft state correlation vanishes, consistent with a trend of a decreasing  $\Gamma_H$ - $F_H$  coherence, observed already for the TS state (see also Tables 1 and 2). Concluding, both the PH and PS states are characterized by a vanishing short-term  $\Gamma_H$ - $F_H$  correlation. This extends a definition that can be found in the literature (e.g., Wilms et al. 2001) identifying them with a missing (pure hard) or completely dominating (pure soft) disk component in the soft X-ray spectra.

### 3.4. Hard X-ray - radio correlations

A large set of high quality data in the 22–100 keV band allows us to investigate correlations between the

hard X-ray properties and the radio emission from Cyg X-1 in an unprecedented way. A much higher sensitivity above 20 keV was reached only with the *CGRO/OSSE* detector and currently with the *NuSTAR* satellite, however, their total exposure time spent on Cyg X-1 observations is several orders of magnitude shorter than that of ISGRI. In addition, since the continuous ISGRI observations are separated only by several minutes, there are many science windows that are truly contemporary to the radio observations.

The radio emission is sizably affected by the orbital modulation effect (e.g., Zdziarski 2012). Using the ephemeris data of Gies et al. (2008) we have tested that the RT and AMI data show a general modulation trend when plotted against the orbital phase. This modulation can be well approximated by a sinusoid with a relative amplitude of about  $\pm 15\%$ , very similar to that of Zdziarski (2012). We have applied this correction to the radio data.

In Figures 4(c) and 5(c) we present the 15 GHz flux  $F_R$  as a function of the photon index  $\Gamma_H$  and hard X-ray flux  $F_H$ , respectively. The simultaneity criterion was the radio observation time being within the ISGRI observation period of a given science window. If there were several radio observations within that period, the radio flux was computed as a weighted mean. In total, there are 272 ISGRI science windows with contemporary radio data. We have tested that loosening the hard X-ray - radio simultaneity criterion from zero to several hours results in an almost unchanged relative data scatter, despite the sample for each state being increased by a factor of several. Therefore it is quite important for the X-ray/radio correlation study to use exactly contemporary data.

There is a limiting value of  $F_H$  seen in Fig. 5(c) around  $80 \times 10^{-10} \text{ erg s}^{-1} \text{ cm}^{-2}$  separating the high and low radio flux levels. This value of  $F_H$  is quite close to the value separating the hard and soft regimes in the  $\Gamma_H$ - $F_H$  density diagram (Fig. 3). The highest radio fluxes are observed for medium level hard X-ray fluxes, whereas for the highest X-ray fluxes there is a slight anticorrelation between  $F_H$  and  $F_R$ . A similar behavior can be noticed in the literature (Gleissner et al. 2004; Wilms et al. 2006; Zdziarski et al. 2011), however, a pattern of  $F_R$  increasing and then decreasing with increasing  $F_H$  shown in Fig. 5(c) is more clearly visible.

A more interesting correlation/anticorrelation pattern is seen in Fig. 4(c) where the radio flux is plotted against the hard X-ray photon index  $\Gamma_H$ . General trend of the radio flux dependence on  $\Gamma_H$  is quite similar to that shown by Böck et al. (2011), where the 15 GHz flux is plotted against the soft X-ray ( $\lesssim 10 \text{ keV}$ ) photon index. However, the  $F_R$  dependence on the hard X-ray pho-

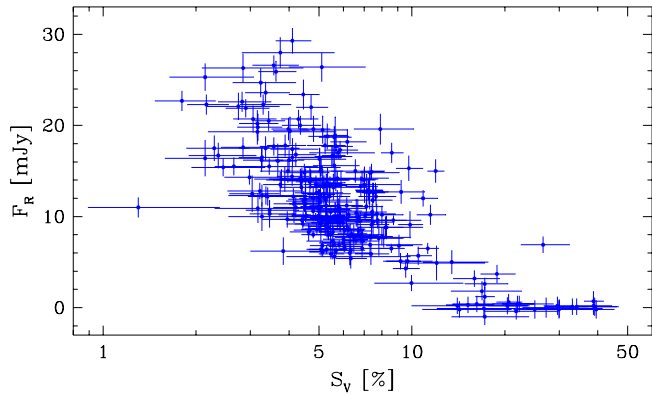


**Figure 6.** RT/AMI radio flux at 15 GHz,  $F_R$ , plotted against the fractional hard X-ray variability amplitude  $S_V$ .

ton index shows some stratification for the three harder states. Radio emission during the PH state varies in a relatively narrow, medium-flux band between 6 and 13 mJy, except for several points. Then, during the TH state  $F_R$  varies around about two times higher level. The highest  $F_R$  values are observed for the HI state, being on average similar to the TH state but showing the largest radio emission variability (see Table 1). Then, the radio flux slowly decreases with an increasing hard X-ray photon index, vanishing above  $\Gamma_H = 2.5$ . A statistically significant correlation between  $F_R$  and  $\Gamma_H$  is found for the PH (positive) and HI and TS (both negative) states, as shown in Table 2. A quite strong  $F_H$ - $F_R$  anticorrelation appears only for the PH state.

The radio flux  $F_R$  plotted in Fig. 6 against  $S_V$  shows a clear overall anticorrelation, with much stronger hard X-ray variability at very low radio fluxes and slowly decreasing variability with increasing radio emission for intermediate and hard states. It is rather surprising that the strongest, flaring radio emission is associated with the weakest plasma variability. Unfortunately, we cannot investigate this issue further: although there were several strong radio flares observed early in the studied period (see Fig. 1(g)), they were not exactly contemporary to the *INTEGRAL* observations. When individual plasma states are considered, only the HI state shows a very strong  $S_V$ - $F_R$  anticorrelation (see Table 2).

### 3.5. States credibility and stability

The six plasma states exposed by the  $\Gamma_H$ - $F_H$  density diagram in Fig. 3 are separated with a high confidence degree, as demonstrated in Sec. 3.2, except for the HI state. Dependence of the four other parameters on  $\Gamma_H$  presented in Fig. 4 shows mostly a smooth transition between the neighboring states, except for the PH and PS states. To reveal the differences between the states in a quantitative way we determined the average values

of various parameters for each state, listed in Table 1. The weighted mean values confirm a distinct character of each state, in particular confirming strongly a peculiarity of both pure states. The most convincing are the correlation parameters presented in Table 2, revealing with a high statistical credibility a distinct dynamical character of each state. For example,  $\Gamma_H$  and  $S_V$  are very strongly anticorrelated for the PH state, for the TH state these two parameters are completely independent, and for the HI state a strong positive correlation appears. Table 2 provides several cases of a compelling evidence for a changing correlation patterns for each pair of the two adjacent states.

Besides the physical differences of the six plasma states we examined also their repetitiveness. As shown in Fig. 1(e), between MJD 52626 (December 2002) and MJD 55342 (May 2010) Cyg X-1 was mostly in the PH state and then it returned to the same state for MJD 57536–57814 (May 2016 – March 2017). The stability of PS state is less evident due to less abundant and more scattered data. Its broad peak in Fig. 3 is formed mainly by data from MJD 55527–55547 (December 2010) but Cyg X-1 was observed in this state also during other periods, mostly in 2013 and in November 2017. The system returns also to the other plasma states after long breaks. Only the SI state was observed by *INTEGRAL* during a relatively short period of 4 years, appearing at the end of years 2011, 2013, 2014, and 2015, i.e., during major transitions between the hard and soft states.

Transitions between the six plasma states are rather rare and rapid because, as we tested, the single *INTEGRAL* orbit data usually occupy a single state region. To explore this point on an hour-scale period we have computed the numbers of state transitions, assuming a minimal  $\Gamma_H$  change of 0.05, i.e., larger than typical uncertainty of majority of our data. The transition occurrence percentages for each plasma state are presented in Table 1. There were 816 transitions found out of 7820 science windows, i.e., the overall state transition probability was around 0.1. The transition probability increases with the spectral softness, however, for the two softest states the  $\Gamma_H$  uncertainty is larger, potentially causing a false detection. The most characteristic feature of the state transition is that they appear almost always between adjacent states. The pure hard state shows the highest stability (2% transition probability) and the smallest  $\Gamma_H$  changes, whereas the all three soft states are quite unstable (27, 20, and 22% transition probability, respectively). These results agree with the conclusion about the stability of Cyg X-1 spectral states monitored by ASM and MAXI (Grinberg et al. 2013).

**Table 1.** Selection criteria, arithmetic (first row of numbers in each panel) and weighted mean (second row) of parameters characterizing six plasma states of Cyg X-1.  $\Gamma_H$ ,  $F_H$ ,  $S_V$  - photon index, flux and fractional variability amplitude in the 22–100 keV band, respectively,  $F_S$  - the 3–12 keV flux,  $H_S$  - 5–12/3–5 keV hardness ratio,  $F_R$  - flux at 15 GHz,  $r_S$ ,  $P_S$  - Spearman rank order test correlation coefficient and null hypothesis (no correlation) probability, respectively, for short-term  $\Gamma_H$ - $F_H$  correlations. Fraction of of time spent in a given state is given in % in each panel header. Numbers in square brackets are per cent probabilities of transition from a given state to the PH, TH, HI, SI, TS, and PS state, respectively.

$\bar{\Gamma}_H$	$\bar{F}_H$	$\bar{S}_V$	$\bar{F}_S$	$\bar{H}_S$	$\bar{F}_R$	$\bar{r}_S$	$\bar{P}_S$
	$10^{-10} \text{ erg s}^{-1} \text{ cm}^{-2}$	%	$\text{counts s}^{-1} \text{ cm}^{-2}$		mJy		
Pure hard state ( $\Gamma_H \leq 1.78$ ) 33.1% [-,2,0,0,0,0]							
1.70±0.04	158±33	5.9±1.8	0.35±0.08	1.58±0.14	8.9±2.0	0.07±0.34	0.22±0.27
1.702±0.001	156.77±0.02	4.8±0.1	0.354±0.001	1.554±0.002	8.6±0.1	0.082±0.013	0.26±0.03
Transitional hard state ( $1.78 < \Gamma_H \leq 1.93$ ) 21.5% [3,-,4,0,0,0]							
1.85±0.04	134±24	4.7±1.8	0.43±0.08	1.40±0.14	14.2±2.9	0.63±0.16	0.02±0.07
1.850±0.001	133.60±0.03	3.3±0.1	0.416±0.001	1.368±0.002	14.0±0.1	0.707±0.012	(19±8)×10 <sup>-5</sup>
Hard intermediate state ( $1.93 < \Gamma_H \leq 2.29$ , $F_H \geq 75 \times 10^{-10} \text{ erg cm}^{-2} \text{ s}^{-1}$ ) 18.7% [0,4,-,4,1,0]							
2.05±0.08	114±25	5.9±2.4	0.56±0.16	1.14±0.14	15.0±6.0	0.72±0.14	0.004±0.015
2.040±0.001	110.98±0.03	4.0±0.1	0.565±0.001	1.097±0.001	14.1±0.1	0.809±0.009	(5±2)×10 <sup>-5</sup>
Soft intermediate state ( $1.93 < \Gamma_H \leq 2.29$ , $F_H < 75 \times 10^{-10} \text{ erg cm}^{-2} \text{ s}^{-1}$ ) 5.6% [0,0,2,-,22,3]							
2.18±0.07	49±16	12.2±5.5	0.50±0.13	0.82±0.12	5.0±1.9	0.67±0.19	0.05±0.10
2.186±0.002	49.60±0.05	7.3±0.5	0.447±0.001	0.815±0.002	4.6±0.4	0.69±0.03	0.005±0.004
Transitional soft state ( $2.29 < \Gamma_H \leq 2.65$ ) 14.1% [0,0,1,8,-,11]							
2.47±0.10	42±20	19.8±7.2	0.57±0.20	0.79±0.12	1.8±1.8	0.47±0.23	0.09±0.15
2.450±0.002	39.49±0.03	12.8±0.5	0.487±0.001	0.802±0.001	1.7±0.3	0.60±0.02	0.06±0.02
Pure soft state ( $\Gamma_H > 2.65$ ) 7.0% [0,0,0,2,20,-]							
2.84±0.14	21±10	28.4±9.5	0.52±0.15	0.67±0.09	0.0±0.4	0.05±0.26	0.46±0.31
2.797±0.005	19.59±0.04	11.5±0.8	0.428±0.001	0.661±0.002	0.0±0.3	0.005±0.033	0.53±0.09

Another issue tested for the state transition was the flux level at which they occur, depending on the passage direction. For the transient BH systems the q-track is usually observed, with the hard-soft transition occurring at much higher flux levels than the soft-hard transition. In our data we have not found evidence for such behavior: differences in the mean  $F_H$  flux for both transition directions are much smaller than the standard deviation of that mean for each pair of the states.

### 3.6. Hard X-ray photon index distribution

At the end of this section we explore whether the finding of clustered photon index values could be obtained with other hard X-ray missions. There are several other past or current hard X-ray detectors that can be used for such a study. Among the two CGRO detectors, OSSE and BATSE, only the latter provided a large set of data in a similar energy band. However, its occultation data are of much lower quality than those of ISGRI. The Beppo-SAX mission has provided a rather limited number of pointed observations of Cyg X-1. The

same is true for the HXD detector of Suzaku and for the most sensitive hard X-ray detectors ever launched, namely those onboard of *NuSTAR*. On the other hand, the Swift BAT detector, characterized by a sensitivity similar to ISGRI, observes Cyg X-1 almost every day but its data are affected by a relatively large statistical uncertainty due to the effectively short observing period for a single day. The most promising seems to be an analysis of the *RXTE* PCA and HEXTE detectors spectra, however it is a rather demanding task, beyond the scope of this paper.

Nevertheless, we have chosen the BATSE detector to get some hint about how its results for Cyg X-1 compare to those of ISGRI. Using the BATSE data has allowed us to extend the observing period by 9 additional years, namely 1991–2000. The 2703 BATSE daily spectra for that period were analyzed with the power-law model. The uncertainty in the BATSE photon index is almost always larger than 0.05 whereas the corresponding uncertainty in the ISGRI data is almost always smaller than this value. This explains why in our test we have

**Table 2.** Pearson correlation coefficient (first row of numbers in each panel) and logarithm of the null hypothesis probability (second row) computed for various pairs of parameters characterizing the six plasma states of Cyg X-1. Correlations for parameter  $r_S$  were computed for the revolution-averaged  $\Gamma_H$  and  $F_H$  data. The parameter symbols are explained in the caption to Table 1. We classify a given correlation as strong when its probability is above 0.99, i.e., when the logarithm of the null hypothesis probability is below -2.

$\Gamma_H-F_H$	$\Gamma_H-F_S$	$\Gamma_H-H_S$	$\Gamma_H-S_V$	$\Gamma_H-r_S$	$\Gamma_H-F_R$	$F_H-H_S$	$F_H-S_V$	$F_H-r_S$	$F_H-F_R$	$S_V-F_R$
Pure hard state										
$-0.09^{+0.03}_{-0.04}$	$0.25^{+0.07}_{-0.08}$	$-0.06^{+0.10}_{-0.08}$	$-0.22^{+0.04}_{-0.04}$	$0.14^{+0.26}_{-0.27}$	$0.38^{+0.18}_{-0.21}$	$0.11^{+0.08}_{-0.08}$	$0.08^{+0.03}_{-0.04}$	$0.15^{+0.25}_{-0.27}$	$-0.35^{+0.21}_{-0.19}$	$-0.23^{+0.17}_{-0.21}$
-6.0	-8.7	-0.93	-32	-0.51	-3.1	-2.2	-4.7	-0.55	-2.7	-1.4
Transitional hard state										
$-0.11^{+0.05}_{-0.05}$	$0.49^{+0.06}_{-0.06}$	$-0.39^{+0.06}_{-0.07}$	$0.02^{+0.05}_{-0.05}$	$0.39^{+0.28}_{-0.38}$	$-0.29^{+0.24}_{-0.20}$	$0.01^{+0.08}_{-0.08}$	$0.21^{+0.05}_{-0.05}$	$0.11^{+0.36}_{-0.39}$	$-0.07^{+0.23}_{-0.24}$	$-0.17^{+0.25}_{-0.22}$
-5.1	-38	-23	-0.4	-1.4	-1.8	-0.09	-6.7	-0.23	-0.27	-0.74
Hard intermediate state										
$-0.30^{+0.05}_{-0.05}$	$0.49^{+0.06}_{-0.06}$	$-0.65^{+0.05}_{-0.04}$	$0.23^{+0.05}_{-0.06}$	$-0.05^{+0.36}_{-0.34}$	$-0.41^{+0.19}_{-0.16}$	$0.33^{+0.07}_{-0.08}$	$-0.13^{+0.06}_{-0.06}$	$0.64^{+0.17}_{-0.27}$	$0.25^{+0.18}_{-0.20}$	$-0.63^{+0.14}_{-0.11}$
-30	-37	-99	-14.3	-0.09	-4.1	-15	-5.0	-4.1	-1.8	-10
Soft intermediate state										
$-0.04^{+0.10}_{-0.10}$	$0.20^{+0.13}_{-0.14}$	$-0.07^{+0.14}_{-0.14}$	$0.24^{+0.11}_{-0.11}$	$0.15^{+0.82}_{-1.10}$	$-0.15^{+0.90}_{-0.71}$	$0.50^{+0.09}_{-0.12}$	$-0.53^{+0.09}_{-0.08}$	$0.6^{+0.4}_{-1.4}$	$0.15^{+0.70}_{-0.90}$	$-0.3^{+0.6}_{-1.0}$
-0.35	-2.3	-0.48	-4.5	-0.07	-0.11	-13	-22	-0.44	-0.11	-0.24
Transitional soft state										
$-0.17^{+0.06}_{-0.06}$	$0.08^{+0.08}_{-0.08}$	$-0.29^{+0.08}_{-0.08}$	$0.34^{+0.06}_{-0.06}$	$-0.44^{+0.40}_{-0.28}$	$-0.82^{+0.43}_{-0.14}$	$0.52^{+0.07}_{-0.07}$	$-0.30^{+0.05}_{-0.06}$	$0.41^{+0.29}_{-0.45}$	$0.43^{+0.40}_{-0.70}$	$-0.23^{+0.74}_{-0.45}$
-7.3	-1.3	-12	-28	-1.5	-2.4	-39	-22	-1.3	-0.67	-0.26
Pure soft state										
$-0.24^{+0.08}_{-0.07}$	$-0.12^{+0.12}_{-0.11}$	$-0.18^{+0.12}_{-0.10}$	$0.04^{+0.09}_{-0.09}$	$-0.11^{+0.55}_{-0.50}$	$0.10^{+0.48}_{-0.53}$	$0.67^{+0.06}_{-0.07}$	$0.10^{+0.09}_{-0.06}$	$-0.27^{+0.58}_{-0.43}$	$0.27^{+0.42}_{-0.55}$	$0.30^{+0.40}_{-0.55}$
-7.9	-1.5	-2.7	-0.43	-0.16	-0.15	-40	-1.7	-0.45	-0.48	-0.55

obtained a distribution of the BATSE photon index resembling a broad, single Gaussian with an additional tail corresponding to the intermediate and soft states, shown in Fig. 7(a). We have also checked that selecting subsamples of the BATSE results with lower  $\Delta\Gamma_H$  values still produces a distribution without any evident clustering.

The comparison between ISGRI and BATSE is also affected by an issue of the need to sum up the BATSE occultation data for a single day to improve the quality of the spectra. Any significant intraday variability of the spectral shape can affect the  $\Gamma_H$  distribution, washing out its discrete features. We have tested the robustness of our results against this concern repeating the ISGRI spectral modeling for 579 daily-summed spectra. As demonstrated in Fig. 7(b), the positions of all states' peaks remained almost unchanged, when compared with the 2D distribution shown in Fig. 3.

Since the *INTEGRAL* satellite hosts another hard X-ray instrument on its board, the SPI imager, it is possible to test the  $\Gamma_H$  clustering with the data taken at the same time as ISGRI data. We analyzed the SPI spectra with the power-law model in the 22–100 keV band. The number of the SPI spectra is much smaller than the number of the ISGRI spectra (due to an exclusion of data with the photon index uncertainty  $> 0.1$ ,

see Sec. 2.1), mostly eliminating the softer states' data. The SPI sensitivity below 100 keV is lower than that of ISGRI, resulting in an error of  $\Gamma_H$  typically around 4 times larger than the typical ISGRI uncertainty. Such a difference in the quality of the spectral data resulted in a broadened  $\Gamma_H$  distribution, see Fig. 7(b), quite similar to that produced with the BATSE data. To check the effect of the smearing of the distribution due to a large  $\Gamma_H$  uncertainty, we applied a Gaussian blur with a standard deviation of 0.08 to the ISGRI data. The resulting distribution is presented with a black histogram in Fig. 7(b), clearly showing that a high-precision determination of the photon index is crucial to uncovering its clustering for Cyg X-1.

## 4. DISCUSSION

### 4.1. Spectral and plasma states of Cyg X-1

A classification of the plasma states based on  $\Gamma_H$  should be confronted with a conventional spectral state selection based on the soft X-rays. In Fig. 8 we present a comparison of our state selection with the state definitions of Grinberg et al. (2013) derived with the ASM and MAXI monitors. Since the energy band and quality of monitoring data are both limited, when compared to the spectra from the soft X-ray telescopes, the state classification of Grinberg et al. (2013) was based on a com-

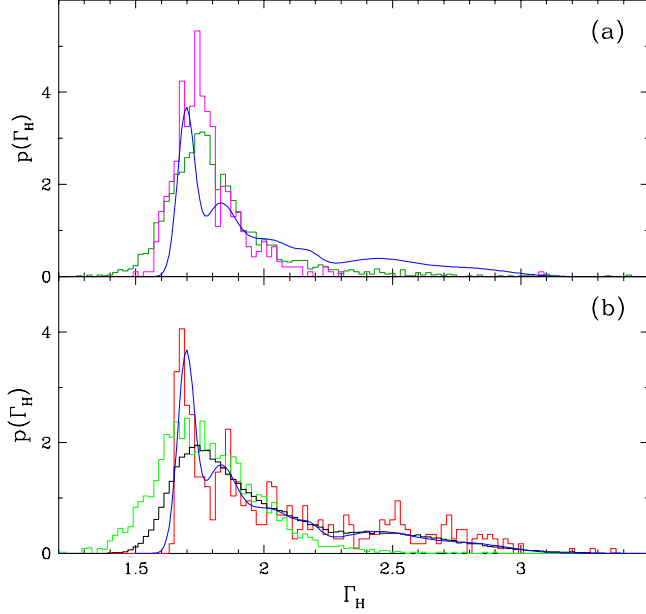


**Figure 7.** Distributions of the 22–100 keV  $\Gamma_H$  parameter obtained with several alternative approaches compared with the six-Gaussian profile (blue curve in each panel). (a) Total (dark green) and selected (magenta, error < 0.06) photon index fitted to the BATSE spectra. (b) Photon index fitted to the SPI spectra (green), photon index fitted to the daily ISGRI spectra (red) and the ISGRI distribution blurred by Gaussian with a standard deviation equal to 0.08 (black).

parison with the results of contemporary *RXTE*/PCA observations. For ASM this gave a good selection of the soft and hard states, whereas the intermediate state was contaminated up to 10%. Selection criteria applied to the MAXI data were more conservative as shown in Fig. 8 where the intermediate state region for MAXI is narrower than the corresponding region for ASM.

We explored the numbers of the soft, intermediate and hard state selections according to the [Grinberg et al. \(2013\)](#) criteria for ASM and MAXI data contemporary to *INTEGRAL* data and classified by a range of the hard X-ray photon index, i.e., data shown with colors in Fig. 8. We observe similar trends as those found by [Grinberg et al. \(2013\)](#), when comparing the all sky monitors state selection with that based on spectral fitting. The PH state data are practically always classified as the hard state. The same happens for the TH state for the MAXI-based selection, whereas for the ASM data we found about 20% data classified as the intermediate state. The HI state is mostly also intermediate with the ASM-based selection but a majority of the HI data fall outside the narrow region of the intermediate state defined with the MAXI criteria. The SI state data are mostly found in the soft state region, 67% for ASM and

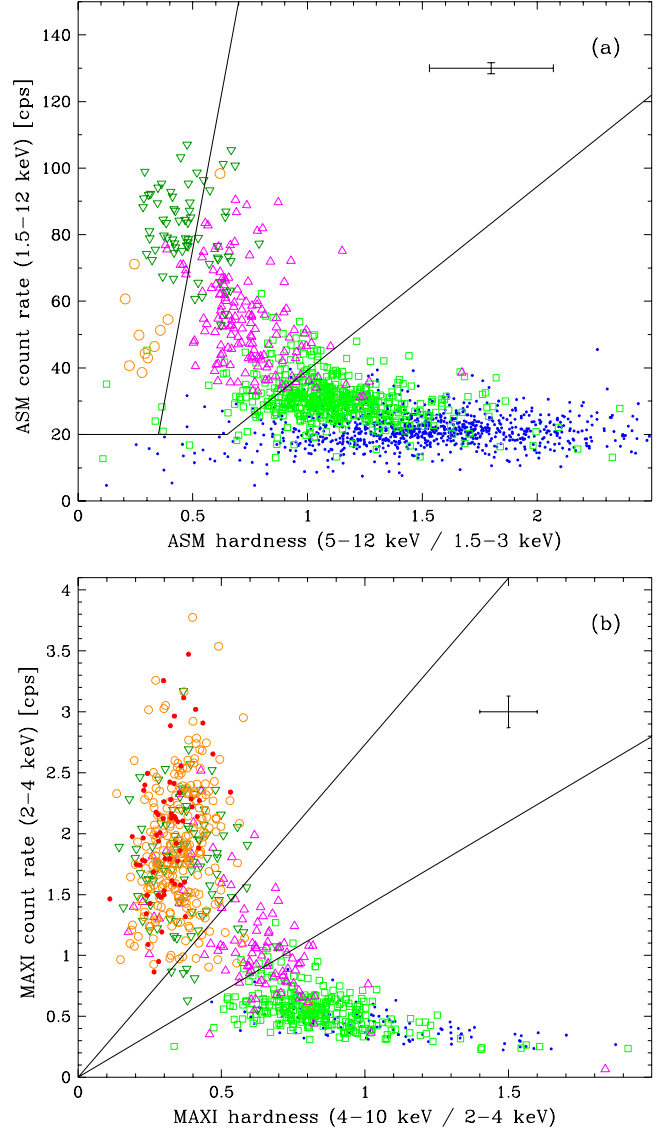


**Figure 8.** Comparison of the state selection based on the soft and hard X-ray criteria. The ASM (a) and MAXI (b) data contemporary to the ISGRI data are marked according to the six plasma states selected with the hard X-ray photon index  $\Gamma_H$  criterion: PH (blue dots), TH (light green squares), HI (magenta triangles up), SI (dark green triangles down), TS (orange circles), and PS (red dots, not observed for ASM). Error bars in each panel show typical errors, the solid lines show the borders of the soft, intermediate and hard spectral state regions according to the [Grinberg et al. \(2013\)](#) state selection criteria.

90% for MAXI. Both TS and PS states data are almost always classified as the soft state with the ASM and MAXI criteria.

As mentioned in Sec. 1, the most reliable state classification is obtained when the spectral slope can be determined directly from the spectra or from monitoring

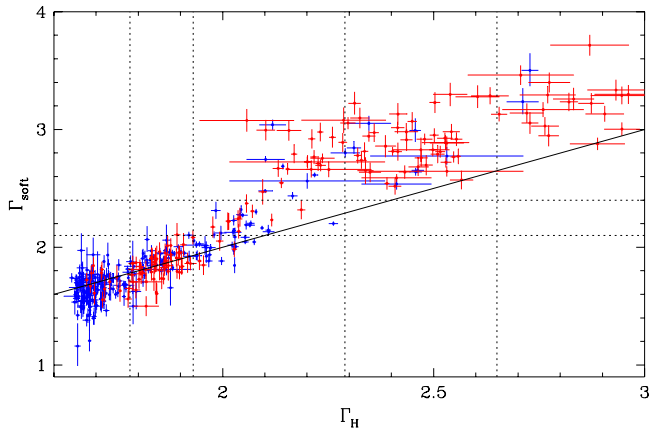


**Figure 9.** Photon index  $\Gamma_{\text{soft}}$  in the 3–12 keV band computed for the ASM (blue) and MAXI (red) daily spectra contemporary to the ISGRI data as a function of the hard X-ray photon index. Vertical dashed lines show the borders of six plasma states found with ISGRI. Horizontal dashed lines show the borders of the hard, intermediate and soft states according to classification of Zdziarski et al. (2002). The solid line is the equality line.

data converted into fluxes in several bands. The second approach was developed e.g., by Zdziarski et al. (2002), where the ASM count rates were converted into flux using a redistribution matrix obtained through a comparison with contemporary PCA spectra. We applied the same procedure to the ASM daily averaged data, using the same matrix and determining fluxes in the three energy bands: 1.5–3.0 keV, 3.0–5.0 keV and 5.0–12.0 keV. With the last two values we determined the photon index in the 3.0–12.0 keV band,  $\Gamma_{\text{soft}}$ . In the case of MAXI we fitted the powerlaw model to the GSC daily spectra obtaining directly the photon index in the same energy band. The  $\Gamma_{\text{soft}}$  results contemporary to the *INTEGRAL* data are shown in Fig. 9, as a function of the hard X-ray photon index  $\Gamma_{\text{H}}$ .

The solid line in Fig. 9 shows that for the PH and TH states there is an agreement between  $\Gamma_{\text{H}}$  and  $\Gamma_{\text{soft}}$ . Data are scattered, at least partly due to the orbital modulated absorption of the soft X-ray emission. For the rest of data the  $\Gamma_{\text{soft}}$  values are larger than the  $\Gamma_{\text{H}}$  values, what can be explained by a disk emission component modulating the soft X-ray part of the spectra.

The relation between the soft and hard X-ray photon indices for Cyg X-1 was studied by Wilms et al. (2006) who analyzed the PCA+HEXTE spectra with an absorbed broken power-law model, with the break energy around 10 keV and the  $\Gamma_1$  and  $\Gamma_2$  indices fitted below and above that energy, respectively. Their model included also a  $K_{\alpha}$  iron line and an exponential cut-off of the high-energy power-law component. Their results

are different from the  $\Gamma_{\text{soft}}$ - $\Gamma_{\text{H}}$  relation shown in Fig. 9, with data lying approximately along a single straight line and  $\Gamma_2$  being always smaller than  $\Gamma_1$ , an effect that was ascribed to a missing reflection component in their model. The difference with respect to our results can be explained by the fact that our  $\Gamma_{\text{H}}$  corresponds to effectively larger energies than the  $\Gamma_2$  fitted by Wilms et al. (2006) because the combined PCA+HEXTE spectra are statistically dominated during the fit by high-quality PCA data below 30 keV. Thus,  $\Gamma_2$  is probing the reflection peak range whereas  $\Gamma_{\text{H}}$ , fitted above 22 keV, is less affected by the reflection component. The soft X-ray photon index  $\Gamma_1$  of Wilms et al. (2006) and Grinberg et al. (2013, 2014) (who, in addition, included the disk component in their model) also cannot be directly compared with our  $\Gamma_{\text{soft}}$  index. Interestingly, the range of their  $\Gamma_1$  values is practically the same as for our  $\Gamma_{\text{soft}}$ , namely between 1.6 and 3.4. The 3–12 keV band is almost not affected by absorption and for the hard state the disk, reflection and iron line components are weak. Thus, for the hardest data  $\Gamma_1$  and  $\Gamma_{\text{soft}}$  should be very similar.

Spectral state classification based on the soft X-ray results, either count rates or fluxes, cannot reveal the six states found with the  $\Gamma_{\text{H}}$  photon index. Figs 8 and 9 demonstrate that the PS, TS and SI states occupy similar range of the soft X-ray parameters. The same holds for the three harder states except for the HI state, roughly traceable through the  $\Gamma_{\text{soft}}$  values. In fact, the definitions of the intermediate state based on the soft X-ray photon index adopted by Zdziarski et al. (2002) (see the horizontal lines in Fig. 9) and Grinberg et al. (2013) ( $2.0 < \Gamma_1 < 2.5$ ) are consistent only with our HI state.

Pottschmidt et al. (2003a) found that in 1998 May the source switched from a typical hard state observed earlier with *RXTE* to a slightly softer hard state. This new hard state exhibited different variability patterns, with a smaller rms amplitude and relatively frequent, failed or successful transitions to the intermediate or soft state. Since the Pottschmidt et al. (2003a) observations were done before the *INTEGRAL* launch, we cannot verify if their bimodal character of the hard state corresponds to our PH and TH states.

An energy-resolved analysis of Cyg X-1 variability with the *RXTE* data taken over the 1999–2011 period (Grinberg et al. 2014) partly covers the period analyzed by Pottschmidt et al. (2003a). This new study confirmed a distinct character of the variability (rms, time lags) observed for the hardest spectra, with  $\Gamma_1 < 1.75$ . As mentioned above, for the hardest data  $\Gamma_1$  and  $\Gamma_{\text{soft}}$  should be very similar, justifying the identification of the hardest

data of Grinberg et al. (2014) with the pure hard state. A much smaller set of Cyg X-1 *RXTE* data was also analyzed in terms of a cross correlation function (CCF) between the photon index and the 3–20 keV count rate at 100 ms time resolution (Skipper et al. 2013). They found that there is an evolution of the CCF from a correlation seen for the hardest spectra changing into an anticorrelation for the rest of the hard state spectra.

In Sec. 1 we mentioned that Cyg X-1 varies in a quite limited region of the HID diagram when compared to the systems undergoing transitions. Our finding is that also in the hard X-ray diagram we do not see a hysteresis: transitions between the states in both directions happen at the same flux level. However, similarly to the transients we found two distinct intermediate states, hard and soft. To the best of our knowledge, bimodality of the intermediate state is almost not explored for Cyg X-1 because in the soft X-rays the HI state just forms the canonical intermediate state, whereas the SI state falls into the soft state region (see Fig. 9). Presumably such a bimodality is seen in the time lags, where for  $2.1 < \Gamma_1 < 2.7$  the lags are much larger than for the rest of the soft state  $\Gamma_1$  range (Grinberg et al. 2014), possibly exposing the soft intermediate state. The SIMS state is characterized by a clearly smaller rms amplitude and this is seen in figs 3 and 4 of Grinberg et al. (2014). A similar effect was already observed by Pottschmidt et al. (2003a) during failed transitions. At hard X-rays we found the opposite behavior: variability amplitude  $S_V$  for the HI state is clearly smaller than for the SI state (see Table 1). The radio emission is rather weak for the SI state and very strong with flares for the HI state, in agreement with the SIMS and HIMS states characteristics (Belloni & Motta 2016). Another similarity is that our HI state occupies quite a wide range of  $\Gamma_H$  as the HIMS does for the hardness ratio, whereas the SI and SIMS regions are quite narrow (see fig. 3.7 of Belloni 2010).

The pure soft state term is used for the spectral state dominated in the soft X-ray band ( $< 20$  keV) by the disk emission (Wilms et al. 2001). Although the state selection adopted in Filothodoros et al. (2018) does not completely correspond to the six states found here, for a summed *INTEGRAL* spectrum of the softest Cyg X-1 data they found the hard/soft compactness ratio,  $l_h/l_s$ , and optical depth of the plasma sharply smaller than the corresponding values for the rest of soft state spectra. Thus, spectral analysis with a hybrid Comptonization model is consistent with a separation of the pure soft state through the  $\Gamma_H$ - $F_H$  diagram.

Provided that the dominant process shaping the hard X-ray continuum of BHBs is inverse Comptonization on thermal electrons, a primary driver of the spectral slope in that band is the system geometry considered in terms of the Compton amplification strength (Haardt & Maraschi 1991; Stern et al. 1995). This amplification can be either modeled directly through a certain parameter of a given implementation of the Comptonization or derived from fluxes of the seed photons and Comptonized component. It has been demonstrated many times that the photon index strongly correlates with the Compton parameter  $y$ , compactness ratio  $l_h/l_s$  or the Compton amplification factor (e.g. Malzac 2001; Wilms et al. 2006; Gierliński et al. 2010). Therefore,  $\Gamma_H$  parameter can be used as a tracer of the system geometry.

The distribution of the  $\Gamma_H$  values found by us for the three harder states is quite similar to those found for Seyfert nuclei (Lubiński et al. 2016). The PH and TH state peaks correspond to radio-quiet Seyferts, having the hardest X-ray spectra and a weak or moderate radio emission. On the other hand, several radio-loud objects of Lubiński et al. (2016) sample exhibit softer spectra resembling the HI state of Cyg X-1. Both photon index distributions, that of Cyg X-1 and that of Seyferts, show an abrupt cut-off below  $\Gamma = 1.7$  (see fig. 3 of Lubiński et al. 2016), i.e., just below the main peak.

Interestingly enough, such a peak of  $\Gamma$  around 1.7 can be justified on a theoretical ground. In their study of the synchrotron boiler effect Malzac & Belmont (2009) found that assuming an initially non-thermal distribution of plasma electrons in the absence of an accretion disk, a quasi-thermal Comptonization continuum can be obtained for a wide range of the plasma compactness, with the photon index close to 1.7. Also their range of  $kT_e$  values, concentrated between 30–50 keV, is similar to that observed for both hard state of Cyg X-1 (Zdziarski et al. 2002; Del Santo et al. 2013) and hard spectra Seyferts (Lubiński et al. 2016). A similar result with a stable spectral slope was obtained by Poutanen & Vurm (2009), who also investigated the synchrotron boiler effect for an initially non-thermal plasma. Therefore, the pure hard state of Cyg X-1 can be interpreted as a limiting mode of accretion dominated by a hot compact plasma, with a negligible interaction with the accretion disk, probably truncated at large radii. The seed photons undergoing Comptonization are produced by a synchrotron radiation of the electrons of the plasma region itself (e.g. Veledina et al. 2011; Poutanen et al. 2018). A quite narrow distribution of  $\Gamma_H$  (or  $y$ ), peaking at the same value for Cyg X-1 and Seyferts, can indicate that the system geometry is reaching its physical limit,

#### 4.2. System geometry



with the plasma region being concentrated well within the inner radius of the disk.

The pure soft state can be interpreted as a second limiting geometry of the Cyg X-1 accreting system, with no signature for an autonomous plasma region besides the non-thermal flares and atmosphere of the accretion disk. The PS state data dominate the softest (s1) spectrum analyzed by Filothodoros et al. (2018). That spectrum, with the compactness ratio  $l_h/l_s$  of  $0.04 \pm 0.01$ , is softer than any *RXTE* spectrum analyzed by Wilms et al. (2006) and Gierliński et al. (2010), with all values of this parameter  $> 0.2$ . On the other hand, there were extremely soft spectra of Cyg X-1 observed by *Suzaku* in 2010 and 2013, contemporary to our PS state. The softest of these was fitted with  $l_h/l_s = 0.11^{+0.02}_{-0.01}$  (Kawano et al. 2017), however, a closer comparison is impossible, due to several parameters fixed at different values than in Filothodoros et al. (2018) and the *Suzaku* spectrum fitted in the 0.8–60 keV band, whereas the *INTEGRAL* spectra were fitted in the 3–200 keV band. The fact that the PH state was not observed with *RXTE* can be explained by much larger time spent by Cyg X-1 in the soft state in the 2010–2017 period than during the *RXTE* observations.

In summary, the Cyg X-1 system appears to evolve between the two extreme plasma states with (primarily for the TH state) non-thermal electrons, whereas for the four transient states the plasma is mostly thermal. States change presumably due to the changes of geometry of the plasma-disk system, resulting in a varying cooling of the plasma by the disk photons. The fact that this evolution goes through several distinct plasma states instead of some gradual transformation demands an explanation. Collecting new *INTEGRAL* data in the coming years will shed more light on the location of these states in the  $\Gamma_H$ - $F_H$  diagram, especially those less populated. Among the four transient states the most intriguing appears the soft intermediate state, showing vertical orientation in Fig. 3. This vertical structure has a width comparable with the typical uncertainty of  $\Gamma_H$  in this range of the diagram. Thus, the intrinsic scatter of the photon index is presumably quite small, indicating a well defined geometry of the hard-to-soft regime transition, a kind of some "bottleneck" mechanism.

Since clustering is observed for both hard and soft regimes, its origin might be a certain common mechanism forming different plasma geometries. A varying accretion rate is thought to be a principal driver of the state transition in binary systems. Nevertheless, even if the system accretes at distinct rates, these rates should be well preserved during the mass transport in the disk. In addition, there should be a tight mechanism of form-

ing specific plasma geometries in a reaction to a varying accretion rate. More light on the plasma states in Cyg X-1 will be shed after state-wise broad-band spectral analysis with physical models and more advanced timing analysis.

## 5. CONCLUSIONS

We have analyzed *INTEGRAL*/ISGRI data collected over 15 years of Cyg X-1 observations, exploring all uninterrupted monitoring periods, lasting typically 0.5–2 hour. This data set comprised almost 8000 pointings for which we have extracted spectra and computed the fractional variability amplitude. Since the emission of Cyg X-1 in the 22–100 keV is unabsorbed and weakly affected by the Compton reflection and high-energy thermal cut-off, even a simple power-law model allows for a reliable characterization of the primary emission from the hot plasma. Using this model we determined the flux  $F_H$  and photon index  $\Gamma_H$  for the 22–100 keV band. To explore the hard X-ray/radio relation we used the RT/AMI data at 15 GHz. Our main findings are as follows:

1. The  $\Gamma_H$ - $F_H$  density diagram reveals six distinct regions, concentrated around  $\Gamma_H = 1.7, 1.85, 2.0, 2.2, 2.5$  and  $2.8$ , with a relative population of 33%, 21%, 19%, 6%, 14% and 7%, respectively. These six plasma states of Cyg X-1 were named, accordingly, pure hard, transitional hard, hard intermediate, soft intermediate, transitional soft and pure soft state. Such clustering is observed for the first time for any BH binary.
2. Each of the six plasma states exhibits a different range of variability measured with the fractional variability amplitude  $S_V$ . In the three softer states the mean  $S_V$  is typically  $\gtrsim 10\%$ , whereas for the three harder states it is typically  $\lesssim 5\%$ , reaching minimal values for the transitional hard state. Our results extend to higher energy the findings of Grinberg et al. (2014), who found for Cyg X-1 a minimal variability for medium hardness data at several energy bands below 15 keV. This trend is different from the typical behavior observed in soft X-rays for transient BHBs, where the variability increases monotonically with the spectral hardness.
3. The radio flux  $F_R$  at 15 GHz is correlated with all three hard X-ray observables. An overall correlation with the maximal radio fluxes seen for an intermediate range of hard X-ray flux and spectral slope values, was already reported for Cyg X-1. However, the radio flux plotted against the hard photon index occupies different levels for all six states. In addition, we found that the radio flux decreases with an increasing hard X-ray variability amplitude  $S_V$ .

4. We have confronted our plasma states with the standard spectral states selected using the softer X-ray bands. We identify the pure hard and transitional hard states with the two hard states found by Pottschmidt et al. (2003a) and Grinberg et al. (2014), both using the soft X-rays. A distinction between the two intermediate states for Cyg X-1 is made for the first time, they appear to be counterparts of the HIMS and SIMS states observed typically for BHB transients. The pure soft state was identified within the soft state through its specific hard X-ray variability.

5. Under the assumption of the Comptonization process as a primary source of the hard X-ray radiation our results can be interpreted in terms of six distinct geometries of the plasma region in Cyg X-1. The hardest and softest states show no hour-scale  $F_H$ - $\Gamma_H$  correlation, suggesting a lack of plasma-accretion disk interaction. The other four states exhibit strong correlation, slowly decreasing with increasing  $\Gamma_H$ , presumably due to decreasing inner radius of the disk.

6. Our results for the pure hard state agree with the predictions of the synchrotron boiler models, with primarily non-thermal hot electrons Comptonizing their own synchrotron radiation. Such models predict also a narrow distribution of the photon index for a broad

range of the system parameters, in agreement with our findings.

## ACKNOWLEDGMENTS

This research was based on observations with *INTEGRAL*, an ESA project with instruments and science data centre funded by ESA member states (especially the PI countries: Denmark, France, Germany, Italy, Switzerland, Spain), the Czech Republic, and Poland and with the participation of Russia and the USA. We have been supported by the Polish National Science Centre (NCN) grant 2014/13/B/ST9/00570 (AF,PL) and grant 2015/18/A/ST9/00746 (AAZ). This research has made use of MAXI data provided by RIKEN, JAXA and the MAXI team. We thank the reviewer for his/her thorough review and highly appreciate the comments and suggestions, which significantly contributed to improving the quality of the publication.

*Facilities:* INTEGRAL(IBIS,JEM-X,SPI),AMI, RXTE(ASM),MAXI,Swift(BAT),CGRO(BATSE).

*Software:* OSA v10.2 and 11.0 (Courvoisier et al. 2003), mxproduct (Matsuoka et al. 2009), HEASOFT (HEASARC 2014), XSPEC (v12.9.0; Arnaud 1996)

## APPENDIX

### A. SEPARATION OF THE TWO SOFT STATES

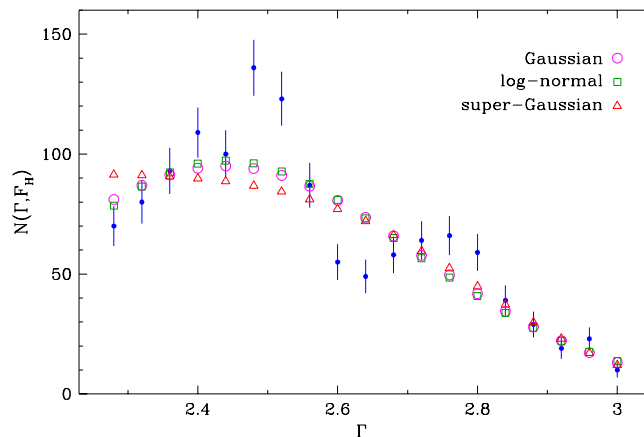


**Figure 10.** Projection of the  $\Gamma_H - F_H$  diagram data on the  $\Gamma_H$  axis. Number of points within a rectangular region centered at given  $\Gamma_H$  is shown in blue. Fitted distributions are shown with symbols without error bars.

The number of  $\Gamma - F_H$  data missing in the valley between the transitional soft and pure soft states was determined using rectangular regions with the longer side perpendicular to the line connecting the centers of these two regions (see Sec. 3.2 and Fig. 3). Figure 10 presents the number of data points found for rectangular regions centered at  $\Gamma_H$  between 2.28 and 3.0, with a step of 0.04. The null hypothesis probability (i.e., a single soft state) was tested

with the three density models: Gaussian, log-normal, and super-Gaussian fitted to the rectangular regions data. The super-Gaussian is a flat-top Gaussian, where the standard Gaussian exponent argument is raised additionally to some power, in our case it was set to 2:  $f(x) \propto \exp\{-[(x - x_0)^2/(2\sigma^2)]^2\}$ . The  $\chi^2$  test values for the log-normal, Gaussian and super-Gaussian models are 62.4, 64.5, and 73.4, respectively, corresponding to  $p$ -values of  $2 \times 10^{-7}$ ,  $9 \times 10^{-8}$ , and  $< 10^{-8}$ , respectively, for 16 degrees of freedom. The valley between the TS and PS states is seen at  $\Gamma_H$  around 2.6. For all tested models at least 60 data points are missing in the valley and must be shifted to either the transitional soft ( $\Gamma_H \approx 2.5$ ) or to the pure soft state ( $\Gamma_H \approx 2.78$ ) peaks.

## B. CLUSTERING TEST WITH THE EQPAIR MODEL

To simulate a set of realistic spectra we used the results of [Filothodoros et al. \(2018\)](#) who fitted the hybrid Comptonization model `eqpair` to the JEM-X and ISGRI spectra of Cyg X-1 in the 3–200 keV band. Their spectra were grouped according to the 40–100/22–40 keV hardness ratio, forming 12 spectral sets, 6 for hard state and 6 for soft state (see fig. 1 in [Filothodoros et al. \(2018\)](#)). Since [Filothodoros et al. \(2018\)](#) and our data cover the same spectral shape range, their hardness ratio range corresponds to our  $\Gamma_H$  range. The leading `eqpair` parameter driving the spectral slope is the hard/soft compactness ratio,  $l_h/l_s$ . Its dependence on the 40–100/22–40 keV hardness found for Cyg X-1 by [Filothodoros et al. \(2018\)](#) is nearly exponential, with  $\log(l_h/l_s)$  between -0.9 and 1.3. Using their results we found that the dependence of the five other main `eqpair` parameters on  $\log(l_h/l_s)$  is practically linear, separately for the hard and soft state. Values of these parameters were computed for 170  $\log(l_h/l_s)$  channels in the [0.45,1.3] range for the hard state, and for 200  $\log(l_h/l_s)$  channels in the [-0.9,0.1] range for the soft state. These five parameters are (with the limits found for the hard and soft state, respectively, given in parenthesis): Thomson scattering depth of the plasma (1.52–0.88, 0.7–0.12), non-thermal/thermal power ratio (0.78–0.51, 0.57–0.31), index of the non-thermal electrons’ power-law distribution (2.04–2.25, 2.13–3.74), Compton reflection strength (0.14–0.6, 1.81–3.42) and the seed photons temperature (150 eV, 150–300 eV). For each simulation we have randomly chosen a spectrum from our 7821 spectra (see Sec. 2.1), using its exposure time and response files to produce a fake spectrum. In total we simulated 300,000 spectra for each of the hard and soft state regimes. The 22–100 keV flux for each channel was randomized with a normal distribution, approximating that observed in Fig. 3.

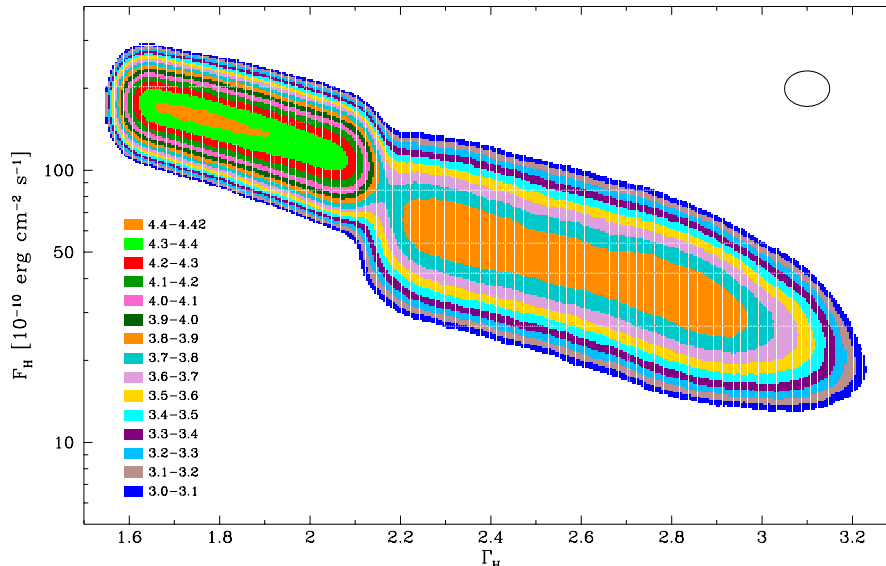


**Figure 11.** Density map of the  $\Gamma_H$ - $F_H$  distribution obtained from the power-law model fitted to the spectra simulated with the `eqpair` model. The ellipse shows the size of the density sampling region.

The simulated spectra were then fitted with the power-law model, producing the set of the  $\Gamma_H$ - $F_H$  results. The corresponding density map is shown in Fig. 11, with a smooth distribution of density for both the hard and soft regimes. We tested various modifications of the functions approximating the dependence of the `eqpair` parameters on

$\log(l_h/l_s)$ . Only small ( $< 10\%$ ) and broad density maxima are occasionally observed. We did not obtain an artificial aggregation of the photon index resembling the six plasma states shown in Fig. 3.

## REFERENCES

- Abramowicz, M. A., Chen, X., Kato, S., Lasota, J., & Regev, O. 1995, *ApJL*, 438, L37, doi: [10.1086/187709](https://doi.org/10.1086/187709)
- Almaini, O., Lawrence, A., Shanks, T., et al. 2000, *MNRAS*, 315, 325, doi: [10.1046/j.1365-8711.2000.03385.x](https://doi.org/10.1046/j.1365-8711.2000.03385.x)
- Begelman, M. C., Armitage, P. J., & Reynolds, C. S. 2015, *ApJ*, 809, 118, doi: [10.1088/0004-637X/809/2/118](https://doi.org/10.1088/0004-637X/809/2/118)
- Belloni, T. M. 2010, in *Lecture Notes in Physics*, Berlin Springer Verlag, Vol. 794, *Lecture Notes in Physics*, Berlin Springer Verlag, ed. T. Belloni, 53
- Belloni, T. M., & Motta, S. E. 2016, in *Astrophysics and Space Science Library*, Vol. 440, *Astrophysics of Black Holes: From Fundamental Aspects to Latest Developments*, ed. C. Bambi, 61
- Böck, M., Grinberg, V., Pottschmidt, K., et al. 2011, *A&A*, 533, A8, doi: [10.1051/0004-6361/201117159](https://doi.org/10.1051/0004-6361/201117159)
- Bowyer, S., Byram, E. T., Chubb, T. A., & Friedman, H. 1965, *Science*, 147, 394, doi: [10.1126/science.147.3656.394](https://doi.org/10.1126/science.147.3656.394)
- Bradt, H. V., Rothschild, R. E., & Swank, J. H. 1993, *AAPS*, 97, 355
- Cabanac, C., Roques, J.-P., & Jourdain, E. 2011, *ApJ*, 739, 58, doi: [10.1088/0004-637X/739/2/58](https://doi.org/10.1088/0004-637X/739/2/58)
- Courvoisier, T. J.-L., Walter, R., Beckmann, V., et al. 2003, *A&A*, 411, L53, doi: [10.1051/0004-6361:20031172](https://doi.org/10.1051/0004-6361:20031172)
- Del Santo, M., Malzac, J., Belmont, R., Bouchet, L., & De Cesare, G. 2013, *MNRAS*, 430, 209, doi: [10.1093/mnras/sts574](https://doi.org/10.1093/mnras/sts574)
- Esin, A. A., McClintock, J. E., & Narayan, R. 1997, *ApJ*, 489, 865, doi: [10.1086/304829](https://doi.org/10.1086/304829)
- Fender, R., & Muñoz-Darias, T. 2016, in *Lecture Notes in Physics*, Berlin Springer Verlag, Vol. 905, *Lecture Notes in Physics*, Berlin Springer Verlag, ed. F. Haardt, V. Gorini, U. Moschella, A. Treves, & M. Colpi, 65
- Filothodoros, A., Lubiński, P., & Zdziarski, A. A. 2018, in *XXXVIII Polish Astronomical Society Meeting*, ed. A. Różańska, Vol. 7, 326–329
- Fraley, C., & Raftery, A. 2002, *Journal of American Statistical Association*, 97, 611, doi: [10.1198/016214502760047131](https://doi.org/10.1198/016214502760047131)
- Gehrels, N., Chincarini, G., Giommi, P., et al. 2004, *ApJ*, 611, 1005, doi: [10.1086/422091](https://doi.org/10.1086/422091)
- Gierliński, M., Zdziarski, A. A., & Done, C. 2010, *ArXiv e-prints*. <https://arxiv.org/abs/1011.5840>
- Gierliński, M., Zdziarski, A. A., Done, C., et al. 1997, *MNRAS*, 288, 958
- Gies, D. R., Bolton, C. T., Blake, R. M., et al. 2008, *ApJ*, 678, 1237, doi: [10.1086/586690](https://doi.org/10.1086/586690)
- Gleissner, T., Wilms, J., Pooley, G. G., et al. 2004, *A&A*, 425, 1061, doi: [10.1051/0004-6361:20040280](https://doi.org/10.1051/0004-6361:20040280)
- Grinberg, V., Hell, N., Pottschmidt, K., et al. 2013, *A&A*, 554, A88, doi: [10.1051/0004-6361/201321128](https://doi.org/10.1051/0004-6361/201321128)
- Grinberg, V., Pottschmidt, K., Böck, M., et al. 2014, *A&A*, 565, A1, doi: [10.1051/0004-6361/201322969](https://doi.org/10.1051/0004-6361/201322969)
- Grinberg, V., Leutenegger, M. A., Hell, N., et al. 2015, *A&A*, 576, A117, doi: [10.1051/0004-6361/201425418](https://doi.org/10.1051/0004-6361/201425418)
- Haardt, F., & Maraschi, L. 1991, *ApJL*, 380, L51, doi: [10.1086/186171](https://doi.org/10.1086/186171)
- Harmon, B. A., Wilson, C. A., Fishman, G. J., et al. 2004, *ApJS*, 154, 585, doi: [10.1086/421940](https://doi.org/10.1086/421940)
- Jones, M. E. 1991, in *Astronomical Society of the Pacific Conference Series*, Vol. 19, *IAU Colloq. 131: Radio Interferometry. Theory, Techniques, and Applications*, ed. T. J. Cornwell & R. A. Perley, 395–399
- Jourdain, E., Götz, D., Westergaard, N. J., Natalucci, L., & Roques, J. P. 2008, in *Proceedings of the 7th INTEGRAL Workshop, PoS(Integral08)144*
- Kawano, T., Done, C., Yamada, S., et al. 2017, *PASJ*, 69, 36, doi: [10.1093/pasj/psx009](https://doi.org/10.1093/pasj/psx009)
- Krimm, H. A., Holland, S. T., Corbet, R. H. D., et al. 2013, *ApJS*, 209, 14, doi: [10.1088/0067-0049/209/1/14](https://doi.org/10.1088/0067-0049/209/1/14)
- Lebrun, F., Leray, J. P., Lavocat, P., et al. 2003, *A&A*, 411, L141, doi: [10.1051/0004-6361:20031367](https://doi.org/10.1051/0004-6361:20031367)
- Levine, A. M., Bradt, H., Cui, W., et al. 1996, *ApJL*, 469, L33, doi: [10.1086/310260](https://doi.org/10.1086/310260)
- Lubiński, P. 2009, *A&A*, 496, 557, doi: [10.1051/0004-6361:200810897](https://doi.org/10.1051/0004-6361:200810897)
- Lubiński, P., Beckmann, V., Gibaud, L., et al. 2016, *MNRAS*, 458, 2454, doi: [10.1093/mnras/stw454](https://doi.org/10.1093/mnras/stw454)
- Malzac, J. 2001, *MNRAS*, 325, 1625, doi: [10.1046/j.1365-8711.2001.04564.x](https://doi.org/10.1046/j.1365-8711.2001.04564.x)
- Malzac, J., & Belmont, R. 2009, *MNRAS*, 392, 570, doi: [10.1111/j.1365-2966.2008.14142.x](https://doi.org/10.1111/j.1365-2966.2008.14142.x)
- Matsuoka, M., Kawasaki, K., Ueno, S., et al. 2009, *PASJ*, 61, 999, doi: [10.1093/pasj/61.5.999](https://doi.org/10.1093/pasj/61.5.999)
- McClintock, J. E., & Remillard, R. A. 2006, *Black hole binaries*, ed. W. H. G. Lewin & M. van der Klis, 157–213
- Narayan, R., & Yi, I. 1994, *ApJL*, 428, L13, doi: [10.1086/187381](https://doi.org/10.1086/187381)

- Natalucci, L., & Savchenko, V. 2017, INTEGRAL/IBIS calibration status, International Astronomical Consortium for High Energy Calibration
- Pottschmidt, K., Wilms, J., Nowak, M. A., et al. 2003a, *A&A*, 407, 1039, doi: [10.1051/0004-6361:20030906](https://doi.org/10.1051/0004-6361:20030906)
- Pottschmidt, K., Wilms, J., Chernyakova, M., et al. 2003b, *A&A*, 411, L383, doi: [10.1051/0004-6361:20031258](https://doi.org/10.1051/0004-6361:20031258)
- Poutanen, J., Veledina, A., & Zdziarski, A. A. 2018, *A&A*, 614, A79, doi: [10.1051/0004-6361/201732345](https://doi.org/10.1051/0004-6361/201732345)
- Poutanen, J., & Vurm, I. 2009, *ApJL*, 690, L97, doi: [10.1088/0004-637X/690/2/L97](https://doi.org/10.1088/0004-637X/690/2/L97)
- Skipper, C. J., McHardy, I. M., & Maccarone, T. J. 2013, *MNRAS*, 434, 574, doi: [10.1093/mnras/stt1044](https://doi.org/10.1093/mnras/stt1044)
- Soldi, S., Beckmann, V., Baumgartner, W. H., et al. 2014, *A&A*, 563, A57, doi: [10.1051/0004-6361/201322653](https://doi.org/10.1051/0004-6361/201322653)
- Stern, B. E., Poutanen, J., Svensson, R., Sikora, M., & Begelman, M. C. 1995, *ApJL*, 449, L13+, doi: [10.1086/309617](https://doi.org/10.1086/309617)
- Tetarenko, B. E., Sivakoff, G. R., Heinke, C. O., & Gladstone, J. C. 2016, *ApJS*, 222, 15, doi: [10.3847/0067-0049/222/2/15](https://doi.org/10.3847/0067-0049/222/2/15)
- Veledina, A., Vurm, I., & Poutanen, J. 2011, *MNRAS*, 414, 3330, doi: [10.1111/j.1365-2966.2011.18635.x](https://doi.org/10.1111/j.1365-2966.2011.18635.x)
- Wilms, J., Nowak, M. A., Pottschmidt, K., et al. 2001, *MNRAS*, 320, 327, doi: [10.1046/j.1365-8711.2001.03983.x](https://doi.org/10.1046/j.1365-8711.2001.03983.x)
- Wilms, J., Nowak, M. A., Pottschmidt, K., Pooley, G. G., & Fritz, S. 2006, *A&A*, 447, 245, doi: [10.1051/0004-6361:20053938](https://doi.org/10.1051/0004-6361:20053938)
- Winkler, C., Courvoisier, T. J.-L., Di Cocco, G., et al. 2003, *A&A*, 411, L1, doi: [10.1051/0004-6361:20031288](https://doi.org/10.1051/0004-6361:20031288)
- Zdziarski, A. A. 2012, *MNRAS*, 422, 1750, doi: [10.1111/j.1365-2966.2012.20754.x](https://doi.org/10.1111/j.1365-2966.2012.20754.x)
- Zdziarski, A. A., Lubiński, P., & Sikora, M. 2012, *MNRAS*, 423, 663, doi: [10.1111/j.1365-2966.2012.20903.x](https://doi.org/10.1111/j.1365-2966.2012.20903.x)
- Zdziarski, A. A., Malyshev, D., Chernyakova, M., & Pooley, G. G. 2017, *MNRAS*, 471, 3657, doi: [10.1093/mnras/stx1846](https://doi.org/10.1093/mnras/stx1846)
- Zdziarski, A. A., Poutanen, J., Paciesas, W. S., & Wen, L. 2002, *ApJ*, 578, 357, doi: [10.1086/342402](https://doi.org/10.1086/342402)
- Zdziarski, A. A., Shapopi, J. N. S., & Pooley, G. G. 2020, *ApJ*, 894, L18, doi: [10.3847/2041-8213/ab8d3b](https://doi.org/10.3847/2041-8213/ab8d3b)
- Zdziarski, A. A., Skinner, G. K., Pooley, G. G., & Lubiński, P. 2011, *MNRAS*, 416, 1324, doi: [10.1111/j.1365-2966.2011.19127.x](https://doi.org/10.1111/j.1365-2966.2011.19127.x)
- Zwart, J. T. L., Barker, R. W., Biddulph, P., et al. 2008, *MNRAS*, 391, 1545, doi: [10.1111/j.1365-2966.2008.13953.x](https://doi.org/10.1111/j.1365-2966.2008.13953.x)